doi:10.1093/mnras/sty2585



A successful 3D core-collapse supernova explosion model

David Vartanyan [®], ^{1★} Adam Burrows, ¹ David Radice [®], ^{1,2} M. Aaron Skinner³ and Joshua Dolence⁴

Accepted 2018 September 10, Received 2018 September 10; in original form 2018 August 31

ABSTRACT

In this paper, we present the results of our three-dimensional, multigroup, multineutrinospecies radiation/hydrodynamic simulation using the state-of-the-art code FORNAX of the terminal dynamics of the core of a non-rotating 16 M_{\odot} stellar progenitor. The calculation incorporates redistribution by inelastic scattering, a correction for the effect of many-body interactions on the neutrino-nucleon scattering rates, approximate general relativity (including the effects of gravitational redshifts), velocity-dependent frequency advection, and an implementation of initial perturbations in the progenitor core. The model explodes within ~ 100 ms of bounce (near when the silicon-oxygen interface is accreted through the temporarily stalled shock) and by the end of the simulation (here, \sim 677 ms after bounce) is accumulating explosion energy at a rate of $\sim 2.5 \times 10^{50}$ erg s⁻¹. The supernova explodes with an asymmetrical multiplume structure, with one hemisphere predominating. The gravitational mass of the residual proto-neutron star at \sim 677 ms is \sim 1.42 M $_{\odot}$. Even at the end of the simulation, explosion in most of the solid angle is accompanied by some accretion in an annular region at the wasp-like waist of the debris field. The ejecta electron fraction (Y_e) is distributed between \sim 0.48 and \sim 0.56, with most of the ejecta mass proton-rich. This may have implications for supernova nucleosynthesis, and could have a bearing on the p- and vp-processes and on the site of the first peak of the r-process. The ejecta spatial distributions of both Y_e and mass density are predominantly in wide-angle plumes and large-scale structures, but are nevertheless quite patchy.

Key words: stars: general – supernovae: general.

1 INTRODUCTION

The neutrino mechanism of core-collapse supernovae (CCSNe) was proposed more than 50 yr ago (Colgate & White 1966), but due to the complexity and exotic character of the environment in which it occurs and the realization that hydrodynamic instabilities and turbulence are crucial to explosion in all but a small subset of progenitor stars, credible confirmation of this mechanism and its observational validation have been frustratingly slow. Along with the requirement to incorporate nuclear and particle physics that does justice to the wide range of relevant neutrino—matter interactions and to the equation of state (EOS) of dense nuclear matter, the centrality of turbulent convective and shock instabilities that break spherical symmetry has necessitated performing theoretical simulations in multiple spatial dimensions. The two-dimensional

¹Department of Astrophysical Sciences, Princeton University, Princeton, NJ 08544, USA

² Institute for Advanced Study, 1 Einstein Dr, Princeton, NJ 08540, USA

³Lawrence Livermore National Laboratory, PO Box 808, Livermore, CA 94551-0808, USA

⁴CCS-2, Los Alamos National Laboratory, PO Box 1663, Los Alamos, NM 87545, USA

⁽²D) simulations (axisymmetric) of the 1990s lacked detailed neutrino physics, but demonstrated the relevance of neutrino-driven convection (Herant et al. 1994; Burrows, Hayes & Fryxell 1995). The early years of this millennium introduced another instability [the standing-accretion shock instability (SASI); Blondin, Mezzacappa & DeMarino 2003 and subsequent work built on previous 2D efforts by incorporating general relativity (GR, at various levels of approximation), improving the physical fidelity of the neutrino interactions embedded into the codes, enhancing the spatial resolution of the calculations, and carrying simulations out to later physical times. Summaries of some of this history can be found in reviews by Janka (2012), Burrows (2013), Müller (2016), and Janka, Melson & Summa (2016). In fact, progress in understanding the CCSN mechanism has paralleled progress in both physics and computational capability, and such progress has spanned decades. It is only recently that fully three-dimensional (3D) simulations with multigroup neutrino transfer that address all the physical terms and effects, employ state-of-the-art nuclear equations of state, and cal-

^{*} E-mail: dvartany@princeton.edu

culate for a physically significant duration have emerged. Though there is still much work to do, the recent advent of codes that address the full dimensional and physics requirements of the CCSN problem represents a watershed in the theoretical exploration of the supernova mechanism. In this paper, we present one such modern simulation of the explosion in 3D of a $16\,M_\odot$ star, using our new supernova code FORNAX (Skinner, Burrows & Dolence 2016; Radice et al. 2017; Burrows et al. 2018; Skinner et al. 2018; Vartanyan et al. 2018).

State-of-the-art calculations in 3D exploring the mechanism of CCSN explosions have undergone significant evolution and improvement over the years. Sixteen years ago, Fryer & Warren (2002, 2004) used a smoothed particle hydrodynamics code SNSPH to explore the differences between 2D and 3D simulations and the possible role of rapid rotation. They found their 2D and 3D simulations were similar and that rapid rotation modified the driving core neutrino emissions. However, these simulations employed grey radiation, did not include inelastic energy redistribution nor velocitydependent transport effects, and ignored GR effects. Parametrized studies in 3D (Nordhaus et al. 2010; Hanke et al. 2012; Dolence et al. 2013; Couch & O'Connor 2014; Couch & Ott 2015) disagreed on the relative difficulty of explosion in 3D versus 2D. However, these simulations, while boasting improved hydrodynamics algorithms and resolution, used 'lightbulb' neutrino driving and did not employ competitive neutrino transfer and microphysics. Using ZEUS-MP on a low-resolution 3D grid, Takiwaki, Kotake & Suwa (2012) witnessed the explosion of a 11.2 M_{\top} progenitor (Woosley, Heger & Weaver 2002). However, these authors used the sub-optimal IDSA scheme neutrino transport approach (Liebendörfer, Whitehouse & Fischer 2009), which ignores velocity dependence, GR, and inelasticity, stitches together the opaque and transparent realms in an ad hoc fashion, uses the problematic 'ray-by-ray' approach to multi-D transport, and either neglects 'heavy' neutrinos or incorporates them in a 'leakage' format. The ray-by-ray approach used by many early and current studies performs multiple one-dimension transport calculations, in lieu of truly multi-D transport, and thereby ignores the important effects of lateral transport (Skinner et al. 2016).

Using the CHIMERA code, Lentz et al. (2015) witnessed the explosion of a 15 M_{\odot} progenitor star (Woosley & Heger 2007) $\sim\!\!300$ ms after bounce, $\sim\!\!100$ ms later than their 2D simulation. These authors used state-of-the-art microphysics and approximate GR, but used multigroup flux-limited diffusion and the reduced-dimension rayby-ray approach and evolved the inner 6–8 km in spherical symmetry. In addition, they employed the LS220 EOS (Lattimer & Swesty 1991), now known to be inconsistent with known nuclear systematics.

Early low-resolution 3D simulations using the PROMETHEUS-VERTEX code (Hanke et al. 2013; Tamborra et al. 2014) found that the 11.2, 27 (Woosley et al. 2002), and 25 M_{\odot} (Woosley & Heger 2007) non-rotating progenitors did not explode in 3D, while their 2D counterparts did. PROMETHEUS-VERTEX uses state-of-theart neutrino microphysics, a multigroup variable Eddington factor transport algorithm with approximate GR (Marek et al. 2006), but uses the ray-by-ray approximation to neutrino transport. Later, this group (Melson, Janka & Marek 2015a) witnessed the explosion of a zero-metallicity 9.6 M_☉ progenitor in 3D, a model that explodes easily in 1D (Radice et al. 2017). By making a large strangeness correction to the axial-vector coupling constant in PROMETHEUS-VERTEX, Melson et al. (2015b) were able to generate an explosion in 3D of the non-rotating 20 M_O progenitor that did not otherwise explode. However, such a large correction may be inconsistent with nuclear experiment (Ahmed et al. 2012; Green et al. 2017).

Recently, this group (Summa et al. 2018) has found that rapidly rotating progenitor models (Heger, Woosley & Spruit 2005) explode shortly after the accretion of the silicon—oxygen (Si—O) interface. They argue, as do Takiwaki, Kotake & Suwa (2016), that a strong non-axisymmetric spiral mode facilitates explosion in the rapidly rotating context. However, with their default neutrino physics, this group has yet to witness the explosion in 3D of any non-rotating models using PROMETHEUS-VERTEX. Moreover, their 3D models were all calculated using the LS220 EOS.

Using the COCONUT-FMT code in 3D, Müller (2015) witnessed the explosion of the $11.2~M_{\odot}$ progenitor of Woosley et al. (2002) in 3D employing the LS220 nuclear EOS. However, COCONUT-FMT employs simplified multigroup neutrino transport, the ray-by-ray approximation, neglects both velocity dependence in the neutrino sector and inelastic scattering, and cuts out the proto-neutron star (PNS) core. Its virtue is that it incorporates conformally flat GR. Using COCONUT-FMT and a 3D 18 M_{\odot} initial progenitor to provide perturbations, Müller et al. (2017) witnessed what they interpret as a perturbation-aided explosion and the simulation was carried out to an impressive $\sim\!\!2.5~s$ after bounce.

It is only recently that codes with truly multidimensional, multigroup transport, without the ray-by-ray compromise and with stateof-the-art microphysics and approximate or accurate GR, have been constructed and fielded. Roberts et al. (2016) used the adaptivemesh-refinement (AMR) Cartesian code Zelmani with full GR, the M1 moment closure approach, the SFHo nuclear EOS (Steiner, Hempel & Fischer 2013), but without velocity dependence in the transport sector or inelastic scattering, to evolve the 27 M_{\odot} progenitor of Woosley et al. (2002). Using the same code, Ott et al. (2018) explored the 12, 15, 20, 27, and 40 M_{\odot} progenitor models of Woosley & Heger (2007). This team witnessed the low-energy explosion of all models, save the 12 M_{\odot} model. More recently, Kuroda, Takiwaki & Kotake (2016a) have developed a multigroup radiation-hydrodynamic CCSN code with M1 closure, detailed microphysics, and full GR. However, their recent CCSN simulations (Kuroda, Kotake & Takiwaki 2016b) of 11.2, 40 (Woosley et al. 2002), and 15 M_{\odot} (Woosley & Weaver 1995) progenitors were done with grey transport and none of their models exploded. A related code using the FLASH architecture, AMR, state-of-the-art microphysics, approximate GR, and M1 transport more recently witnesses no explosion for a 20 M_☉ progenitor, but noted large asymmetries in the Si and O shells that might dynamically aid explosion (O'Connor & Couch 2018).

In this paper, we present the first results in a series of 3D simulations that employ our new code FORNAX (Skinner et al. 2018). FORNAX is a multigroup, velocity-dependent neutrino transport code that employs the M1 two-moment closure scheme. It incorporates state-of-the-art neutrino microphysics, approximate GR (with gravitational redshifts), inelastic energy redistribution via scattering, and does not employ the ray-by-ray simplification. Furthermore, it uses a dendritic grid that deresolves in angle upon approach to the core, while maintaining good zone sizes. This allows us to include the stellar centre while employing a spherical grid but without incurring an onerous Courant time-step penalty. We find that the $16\,{\rm M}_{\odot}$ progenitor (Woosley & Heger 2007) explodes in 3D, and does so shortly before its 2D counterpart.

Throughout this paper, we explore the dimensional dependence (2D versus 3D) of the explosion properties. We organize the paper as follows: In Section 2, we outline the setup of our simulation. We explore the basic explosion properties in the beginning of Section 3 and the shock evolution in Section 3.1. In Sections 3.2 and 3.3, we explore the explosion energetics and heating rates and the lumi-

nosities and mean energies, respectively. We look at the ejecta composition in Section 3.4, and study PNS convection in Section 3.5. We comment in Section 3.6 on the possibility of the lepton-number emission self-sustained asymmetry (LESA; Tamborra et al. 2014) in our 3D simulation and the lack of the SASI. In Section 4, we conclude with summary comments and observations.

2 NUMERICAL SETUP AND METHODS

The progenitor upon which we focus in this paper is the $16~M_{\odot}$ model of Woosley & Heger (2007) (which was studied in 2D in Vartanyan et al. 2018), and we employ the state-of-the-art multi-D, multigroup radiation/hydrodynamic code FORNAX (Skinner et al. 2018). Earlier supernova work using FORNAX includes Wallace, Burrows & Dolence 2016 (neutrino breakout burst detection), Skinner et al. 2016 (shortcomings of the ray-by-ray approximation in core-collapse simulations), Radice et al. 2017 (low-mass CC-SNe), Burrows et al. 2018 (the role of microphysics in CCSNe), Morozova et al. 2018 (gravitational wave signatures of CCSNe), Vartanyan et al. 2018 (CCSNe from 12 to 25 M_{\odot}), and Seadrow et al. 2018 (neutrino detection of CCSNe).

FORNAX is a multidimensional, multigroup radiation hydrodynamics code originally constructed to study CCSNe and its structure, capabilities, and variety of code tests are described in Skinner et al. (2018). The generalization of the equations to approximate general-relativistic gravity and redshifts is described in Appendix A. In 2D and 3D, FORNAX employs a dendritic grid which deresolves at small radii and in 3D along the ϕ axis to avoid overly restrictive CFL time-step limitations, while at the same time preserving cell size and aspect ratios. Our method of deresolving near the polar axis for 3D simulations allows us to partially overcome axial artefacts seen conventionally in 3D simulations in spherical coordinates (see e.g. Lentz et al. 2015; Müller et al. 2017). FORNAX solves the comoving-frame velocity-dependent transport equations to order O(v/c). The hydrodynamics uses a directionally unsplit Godunov-type finite-volume scheme and computes fluxes at cell interfaces using an HLLC Riemann solver. For the 3D simulation highlighted in this paper, we employ a spherical grid in r, θ , and ϕ of resolution $608 \times 128 \times 256$. For the comparison 2D simulation, the axisymmetric grid has resolution 608×128 . The radial grid extends out to 10 000 km and is spaced evenly with $\Delta r \sim 0.5$ km for $r \lesssim 50\,\mathrm{km}$ and logarithmically for $r \gtrsim 50\,\mathrm{km}$, with a smooth transition in between. The angular grid resolution varies smoothly from $\Delta\theta \sim 1.9^\circ$ at the poles to $\Delta\theta \sim 1.3^\circ$ at the equator, and has $\Delta\phi\sim 1.4^\circ$ uniformly. For this project, we used a monopole approximation for relativistic gravity following Marek et al. (2006), as described in Appendix A, and employed the SFHo EOS (Steiner et al. 2013), which is consistent with all currently known nuclear constraints (Tews et al. 2017).

We solve for radiation transfer using the M1 closure scheme for the second and third moments of the radiation fields (Vaytet et al. 2011) and follow three species of neutrinos: electron-type (ν_e) , anti-electron-type $(\bar{\nu}_e)$, and ' ν_μ '-type $(\nu_\mu,\,\bar{\nu}_\mu,\,\nu_\tau,$ and $\bar{\nu}_\tau$ neutrino species collectively). We use 12 energy groups spaced logarithmically between 1 and 300 MeV for the electron neutrinos and to 100 MeV for the anti-electron- and ' ν_μ '-neutrinos. The neutrino–matter interactions implemented and the handling of inelastic scattering and energy redistribution of neutrinos off electrons and nucleons are both summarized in Appendix B.

For this paper, we initially evolve collapse in 1D until 10 ms after bounce, and then map to higher dimensions. After mapping, we impose velocity perturbations (for the 2D and 3D, but not 1D,

simulations) following Müller & Janka (2015) in three spatially distinct regions (50–85, 90–250, and 260–500 km), with a maximum speed of 500 km s⁻¹ and harmonic quantum numbers of l=2, m=1, and n=5 (radial), as defined in Müller & Janka (2015). These perturbations were motivated by Müller et al. (2016), who evolve the last minutes of a 3D progenitor and find convective velocities of almost 1000 km s⁻¹ at the onset of collapse (with a corresponding Mach number of 0.1) in the O-shell around 5000 km with a prominent l=2 mode.

Our 3D simulation was evolved to 677 ms after core bounce, and required a total resource burn of \sim 18 million CPU-hours on the NERSC/Cori II machine using 16256 cores in parallel. ¹

We note that the $16\,\mathrm{M}_{\odot}$ progenitor was studied in Vartanyan et al. (2018), but with a different setup. In that paper, we did not include initial velocity perturbations, had 20 (instead of 12) energy bins per neutrino species, and employed an angular resolution of 256 polar cells (instead of 128). We also did not map from 1D to 2D 10 ms after bounce, but evolved entirely in 2D. Our grid then extended to $20\,000\,\mathrm{km}$ (not $10\,000\,\mathrm{km}$). For the 2D comparison model in this paper, we maintain these differences to mimic the setup we use for our concurrent 3D run. However, we obtain the same overall results for the $16\,\mathrm{M}_{\odot}$ progenitor seen in Vartanyan et al. (2018).

3 EXPLOSION PROPERTIES

We find that the $16\,\mathrm{M}_\odot$ progenitor of Woosley & Heger (2007) explodes in both the corresponding 2D and 3D simulations, at $\sim \! 100$ and $\sim \! 120\,\mathrm{ms}$ after bounce, respectively. The corresponding 1D simulation does not explode. The explosions in 2D and 3D are abetted by the inclusion of detailed microphysics — in particular, inelastic scattering off electrons, nucleons, and the associated energy redistribution, and the decrease in the neutral-current neutrino—nucleon scattering rates due to the many-body effect (Horowitz et al. 2017; Burrows et al. 2018) — as well as a steep density gradient at the Si–O interface located deep within the progenitor, near an interior mass of $\sim \! 1.5\,\mathrm{M}_\odot$ (Ott et al. 2018; Vartanyan et al. 2018). Unlike in many recent 3D simulations, we use the SFHo EOS in this work.

At the end of our 3D simulation, ${\sim}677$ ms after bounce, the maximum shock radius has reached ${\sim}5000\,\mathrm{km}$, with an asymptotic velocity of ${\sim}10\,000\,\mathrm{km}\,\mathrm{s}^{-1}$. The diagnostic explosion energy is ${\sim}1.7\,\times\,10^{50}$ erg by this time. The mass of the core ejecta, defined as neutrino-processed gravitationally unbound material, is ${\sim}0.08\,\mathrm{M}_{\odot}$ and growing. The corresponding gravitational PNS mass is ${\sim}1.42\,\mathrm{M}_{\odot}$ and the mean PNS radius ${\sim}29\,\mathrm{km}$. These features are explored in greater detail in the later sections and compared to the results in 2D. In all regards, we find that integrated 3D metrics are significantly less variable with time than their 2D analogues.

In Fig. 1, we show a time sequence of the entropy of the 3D simulation, illustrating the highly non-axisymmetric nature of the explosion. By ~ 100 ms after bounce, shock expansion and explosion are underway, with the outflow initially constituting bubbles interior to the shock. The explosion assumes a bi-cameral structure, with the two hemispheres separated by a plane oriented with $\theta \sim 40^\circ$ and $\phi \sim 50^\circ$ in spherical coordinates. Unlike in 2D, the explosion does not orient around any coordinate axis and there is no axial sloshing; any explosion axis that emerges does so naturally and is not imposed. Indeed, the explosion is not isotropic, but has

 $^{^1}$ For comparison, some earlier 3D simulations (e.g. Summa et al. 2018 for a model with slightly lower resolution, but with rotation.) required \sim 50–100 million CPU-hours to evolve to 0.5 s after bounce.

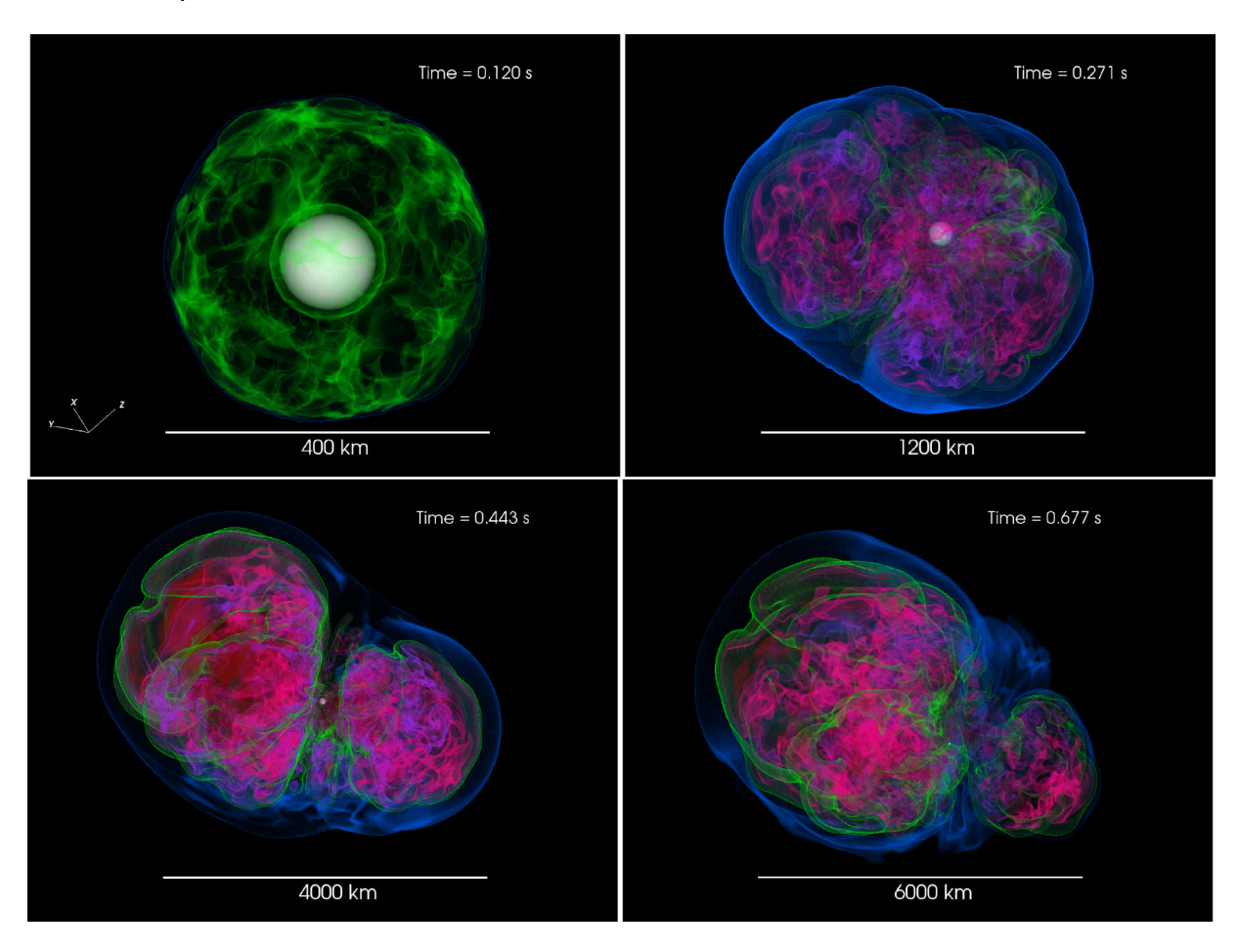


Figure 1. Time sequence of the entropy of the $16 \, \rm M_{\odot}$ progenitor. Note the different spatial scales. The inner white sphere is a $10^{11} \, \rm g \, cm^{-3}$ isosurface that roughly delineates the PNS, and the blue veil traces an entropy contour of 4- k_b /baryon, a proxy for the shock radius. Note the bifurcated cerebral structure of the explosion plumes, with one dominant hemisphere (on the left in this projection). Several 'fingers' are also visible along the axis, though these are accreted shortly after. Note the high-entropy regions (dark red) both along the outer cusps of the plumes and in the interior as matter is funnelled on to the PNS.

a preferred direction, clockwise-orthogonal to the dividing plane. The left hemisphere (in this projection) dominates and we see some fingers along the axis at \sim 443 ms (3rd panel), but these are accreted soon after. The electron distribution follows the entropy distribution, with high Y_e ($Y_e > 0.53$) concentrated along the outer cusps of each plume (see Section 3.4). We see high- Y_e material in both plumes as well as in the interior.

We show in Fig. 2 a volume rendering of the entropy per baryon showing the morphology of the explosion of the 11 $\rm M_{\odot}$ progenitor from Sukhbold, Woosley & Heger (2018) from an upcoming paper (Radice et al. 2018). The snapshot is taken at \sim 690 ms after bounce, when the shock wave (blue outer surface in the figure) has an average radius of \sim 3500 km. The explosion behaves similarly to that of the 16 $\rm M_{\odot}$ progenitor we evolve. The shock is expanding quasi-spherically; however, accretion continues on one side of the PNS, while neutrino-driven winds inflate high-entropy bubbles on the other side.

In Fig. 3, we illustrate a time sequence of entropy slices for the 3D simulation of the 16 M_{\odot} progenitor along the x-y plane (top). At early times, shock breakout is driven by multiple smaller bubbles in 3D, as opposed to a few large plumes in 2D. The shock evolution in 3D transitions from quasi-spherical expansion to expansion along an axis, with the axis randomly chosen. By \sim 300 ms after bounce, the plumes in 3D have merged into two distinct larger solid-angle

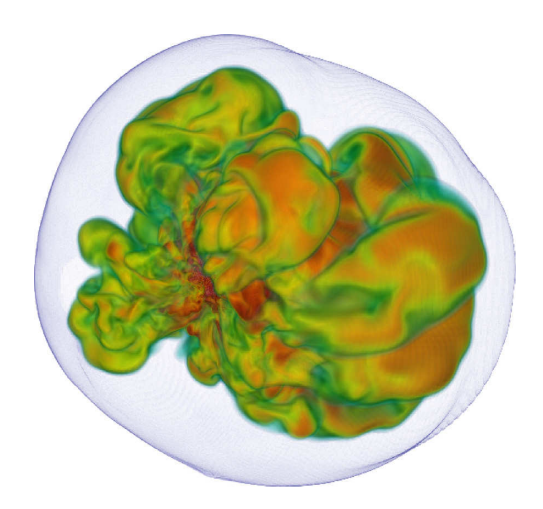


Figure 2. Volume rendering of the entropy per baryon showing the morphology of the explosion of the 11 M_{\odot} progenitor from Sukhbold et al. (2018). The snapshot is taken at \sim 690 ms after bounce, when the shock wave (blue outer surface in the figure) has an average radius of \sim 3500 km. The shock is expanding quasi-spherically, however accretion continues on one side of the PNS, while neutrino-driven winds inflate higher entropy bubbles on the other side.

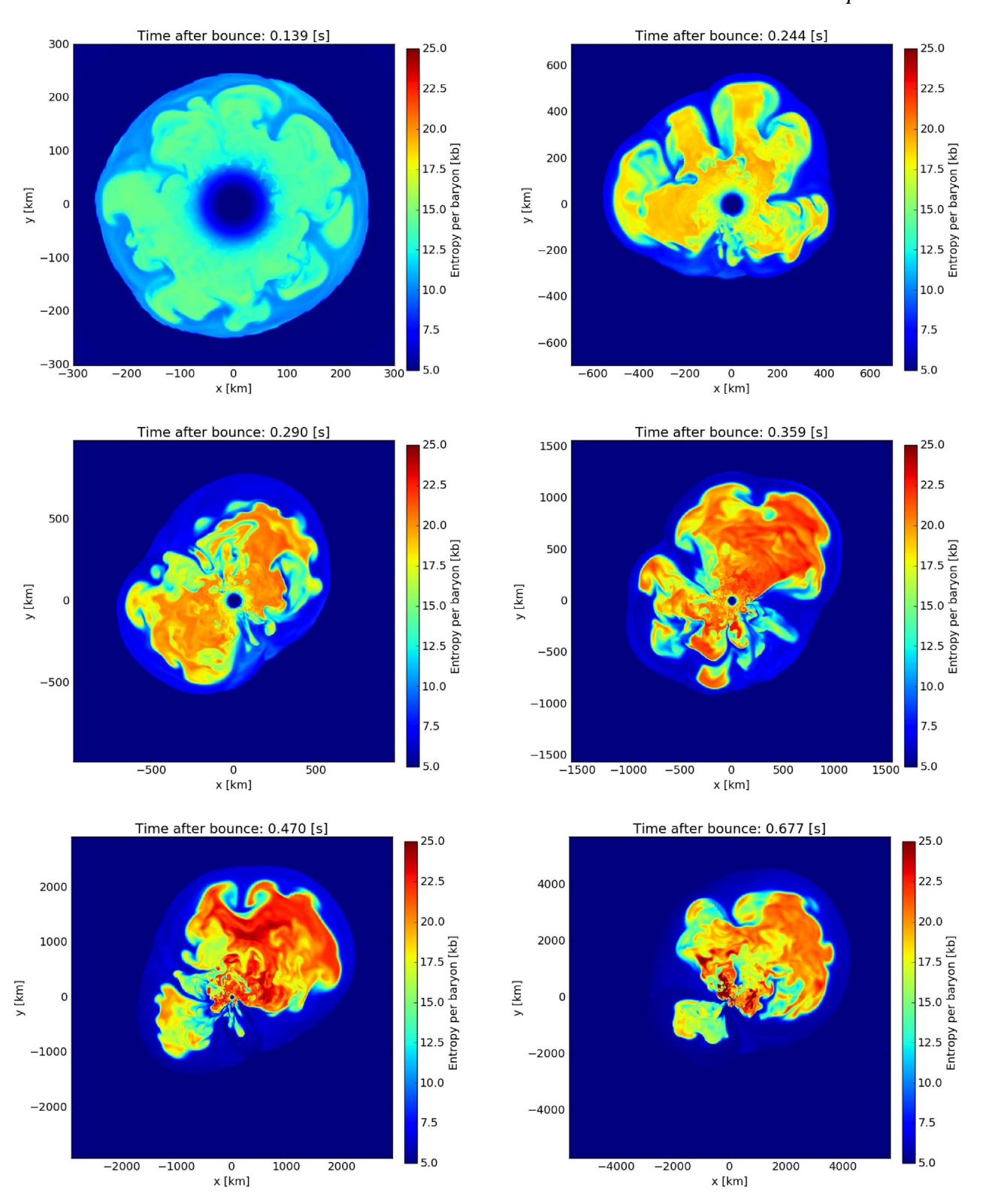


Figure 3. Time sequence slices in the x-y plane illustrating the entropy of the 3D simulation of the 16 M $_{\odot}$ progenitor. Note the changing spatial scales with time. At early times, shock expansion is driven by multiple bubbles, which coalesce into larger plumes. At approximately 300 ms after bounce, we note the development of a dividing axis with two dominant plumes in this slicing. At late times, a single dominant explosion plume emerges, seemingly at the expense of the secondary plume. A persistent wind is present in both plumes initially, and finally, only in the dominant plume. The secondary plume persists and grows, with a characteristic scale of \sim 2000 km, half the size of the primary plume at the end of our simulation. We see simultaneous explosion and accretion. The shock evolution transitions from quasi-spherical expansion to axial expansion, with the axis arbitrarily chosen. See the text for a discussion.

bubbles oriented along a clear axis. We see matter cross and accrete through this axis at earlier times before the explosion settles into the final configuration (see panels 3–5 of Fig. 3). At late times in the 3D simulation, we see the larger plume growing relative to the smaller, leaving a dominant driving plume. This is similar to the behaviour in 2D. A persistent wind that emerges \sim 300 ms after bounce is present in both the large and small explosion plumes, and finally in the dominant plume alone. We see simultaneous explosion and accretion – the smaller plume in Fig. 3 growing relatively in size. Even up to the end of our simulation, some material partially circumnavigates the explosion plumes, plunges inward in a sheet that seems to pinch off the larger from the smaller plume, and is accreted on to the PNS. This accretion pinching in the early explosion phase between the two differently sized exploding plumes resembles a wasp's waist and may be a common feature of some CCSN explosion morphologies. The smaller plume is more prominent in 3D than in 2D, for which at late times the opposing explosion plume's volume ratio is significantly smaller than in 3D.

An inner structure with two counter-ejected large lobes such as we see in this simulation, with one demonstrably larger than the other, crudely resembles the iron ejecta pattern inferred from *XMM* X-ray observations of the supernova remnant (SNR) Cas A (Willingale et al. 2003). This is suggestive, but the remnant structure in any SNR depends upon its entire propagation history through the star's matter field and any apparent morphological association between early and late ejecta patterns could be happenstance. This remains to be determined. However, the rough similarity between our preliminary debris field morphology and the inferred inner mass density and composition patterns from X-ray data is indeed intriguing.

The 3D simulation has lower maximum entropies at late times by \sim 4.5 units (Boltzmann constant ($k_{\rm B}$) per baryon) than its 2D counterpart. However, the entropy averaged over the shocked region (defined where the specific entropy is greater than 4 $k_{\rm B}$ per baryon) is comparable for both simulations. This is because the 3D simulation maintains a more 'isotropic' explosion in that even the subdominant plume subsists, producing comparable mean entropies over the shocked region despite the higher entropies along the dominant axial plume in 2D.

3.1 Shock wave evolution

We find, perhaps surprisingly (Hanke et al. 2012, 2013; Dolence et al. 2013) that our 3D model explodes roughly 50 ms earlier than the corresponding 2D model. In the top panel of Fig. 4, we plot the shock radius versus time after bounce for the 2D (dashed, blue swath) and 3D (solid, green swath). The coloured-in areas indicate the radial spread of the shock location, from minimum to maximum. At the end of our 3D simulation, the mean shock radius has reached beyond $\sim\!5000\,\mathrm{km}$. The 2D model remains roughly spherical in expansion for the first $\sim\!120$ ms, whereas the 3D model deviates from spherical symmetry earlier. We show in the inset a zoomed-in plot of the average shock radii at early times. The shock radii for the 2D and 3D simulations diverge around $\sim\!50$ ms after bounce. The shock of the 3D model barely stalls, while the shock for its 2D counterpart stalls for $\sim\!50$ ms.

In the bottom panel of Fig. 4, we plot the first four spherical harmonics of the shock radius as a function of time after bounce. We take the norm over all orders m and compare 3D (solid) with 2D (dashed). We use the approach outlined in Burrows, Dolence & Murphy (2012) to decompose the shock surface $R_s(\theta, \phi)$ into spher-

ical harmonic components with coefficients:

$$a_{lm} = \frac{(-1)^{|m|}}{\sqrt{4\pi(2l+1)}} \oint R_s(\theta,\phi) Y_l^m(\theta,\phi) d\Omega, \tag{1}$$

normalized such that $a_{00}=a_0=\langle R_s\rangle$ (the average shock radius) and a_{11} , a_{1-1} , and a_{10} correspond to the average Cartesian coordinates of the shock surface $\langle x_s\rangle$, $\langle y_s\rangle$, and $\langle z_s\rangle$, respectively. The orthonormal harmonic basis functions are given by

$$Y_{l}^{m}(\theta,\phi) = \begin{cases} \sqrt{2}N_{l}^{m}P_{l}^{m}(\cos\theta)\cos m\phi & m > 0, \\ N_{l}^{0}P_{l}^{0}(\cos\theta) & m = 0, \\ \sqrt{2}N_{l}^{|m|}P_{l}^{|m|}(\cos\theta)\sin|m|\phi & m < 0, \end{cases}$$
(2)

where

$$N_l^m = \sqrt{\frac{2l+1}{4\pi} \frac{(l-m)!}{(l+m)!}},$$
(3)

 $P_l^m(\cos\theta)$ are the associated Legendre polynomials, and θ and ϕ are the spherical coordinate angles. We plot the norm,

$$P_{\ell} = \frac{\sqrt{\sum_{m=-\ell}^{\ell} a_{\ell m}^2}}{a_{00}} \,. \tag{4}$$

Up to \sim 70 ms after bounce, the $\ell = 2$, 4 moments dominate, the former due to the initial quadrupolar velocity perturbations imposed. From \sim 100 to \sim 200 ms, all moments are comparable in magnitude. Note that the dip in the quadrupole moment at \sim 300 ms corresponds to the dip in mean shock radius seen in the left-hand panel. Shortly afterwards, the shock surface of the 2D simulation rapidly expands, catching up with that of the 3D simulation. At late times, the large-scale, lower ℓ moments dominate. Up to $\ell = 11$ (not shown), we find that the moment magnitudes decrease monotonically with increasing ℓ (and decreasing angular scale). We witness a transition from small structures at early times, coalescing into largescale structures at later times. As the explosion commences, the 3D simulation evinces larger deviations from spherical symmetry than the 2D simulation, as indicated by the larger magnitudes of the respective moments. However, at late times the 2D simulation begins to manifest larger asymmetries than its 3D counterpart, indicated by the larger magnitude of the lower order moments. Both simulations have similar asymptotic shock velocities and maximum shock radii (at a given post-bounce time), though the 2D simulation minimum and average shock radii are roughly \sim 1000 km smaller.

In Fig. 5, we track the dipole orientation of the shock with time. Early on, the shock dipole vector changes sporadically (but does not simply jump up and down as in 2D), but at later times it settles to an axis seemingly chosen arbitrarily. The randomly chosen axis is a defining feature of 3D non-rotating simulations (see e.g. fig. 3 in Burrows et al. 2012). We also see pronounced azimuthal structures in the 3D simulation (as opposed to rings in 2D). Along with the $\ell=0$ explosion mode, the $\ell=1$, m=-1 dipolar mode dominates at late times, and we see such a structure in the 3D explosion maps (Fig. 1).

3.2 Energetics

Before explosion, the energy deposited in the gain region, that thick shellular volume interior to the shock wave where neutrino heating rate exceeds the cooling rate, is most relevant for driving turbulence and establishing the potential for explosion. The larger the energy deposition rate, the closer a given progenitor model is (with its mass accretion rate) to explosion (Burrows & Goshy 1993). However, the total energy deposited in advance of explosion is not related to the

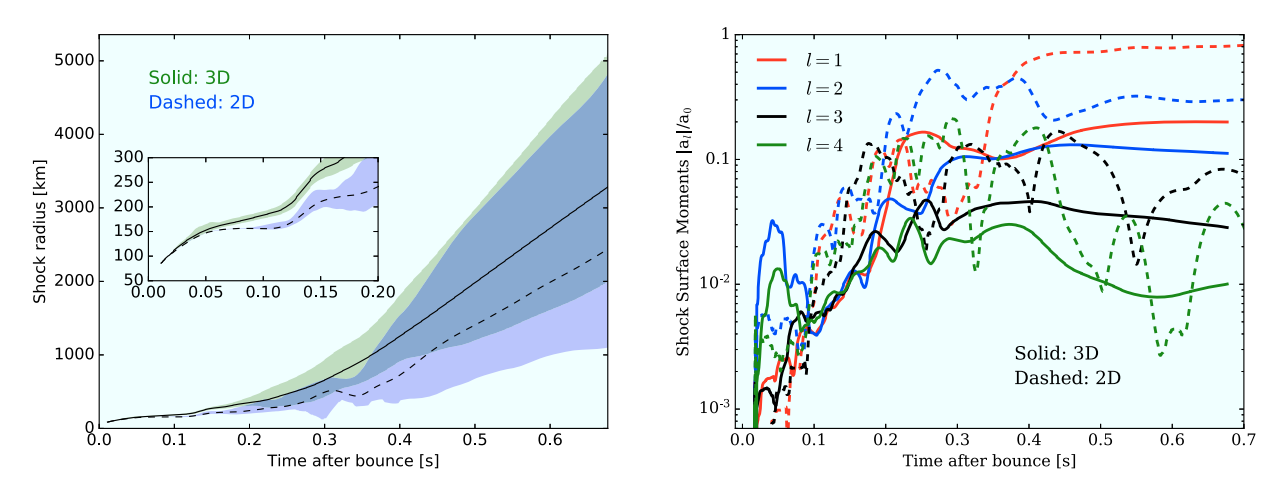


Figure 4. Left: The shock radius (km) versus time after bounce (in seconds) for the 2D (dashed, blue swath) and 3D (solid, green swath). The coloured-in regions indicate the range of the shock location, from minimum to maximum. The 3D simulation explodes slightly earlier. At the end of our simulation, the shock achieves \sim 5000 km. The shock of the 3D model barely stalls in radius, while the shock for its 2D counterpart stalls for \sim 50 ms. We show in the inset a zoomed-in plot of the average shock radii at early times. The mean shock radii for the 2D and 3D simulations have diverged by \sim 50 ms after bounce. Right: The first four spherical harmonic moments of the shock radius as a function of time (in seconds) after bounce, normalized to the mean shock radius (the $\ell = 0$ component). We take the norm over all orders m and compare 3D (solid) to 2D (dashed). Up to \sim 70 ms after bounce, the $\ell = 2$, 4 moments dominate, the former due to the initial quadrupolar velocity perturbations imposed. From \sim 100 to \sim 200 ms, all reduced moments are comparable in magnitude. At late times, the large scale, lower ℓ moments increase in significance. Up to $\ell = 11$ (not shown), we find monotonically decreasing relative moment magnitudes with increasing ℓ (and decreasing angular scale). We see a transition from small structures at early times to large structures at later times. Up to explosion, the 3D simulation evinces much larger deviations from spherical symmetry. At late times, however, the 2D simulation shows much larger asymmetries than the 3D simulation, indicated by the larger magnitude of the reduced moments.

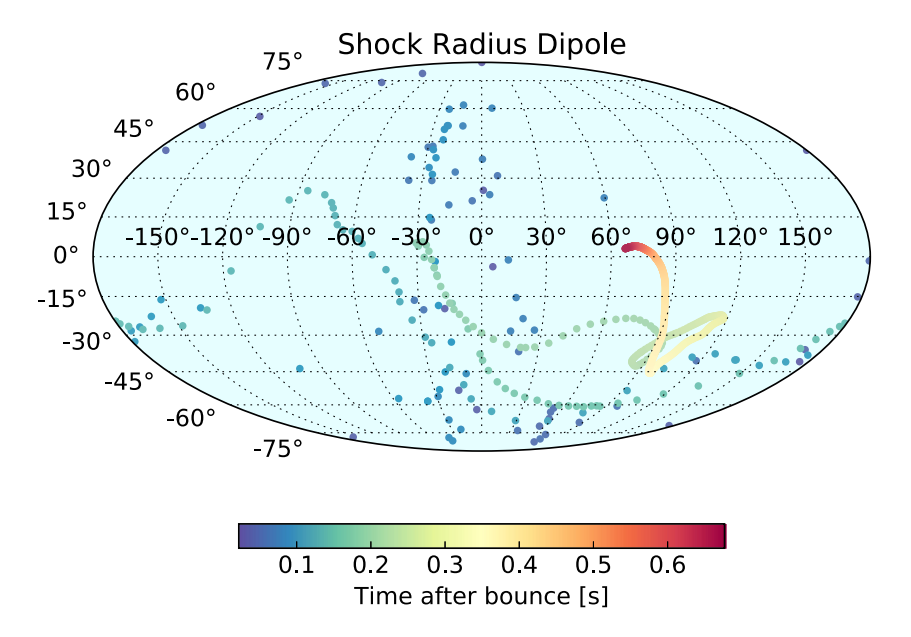


Figure 5. A Mollweide projection of the direction of the shock dipole as a function of time (in seconds) after bounce, colour-coded. Early on, the shock dipolar direction is changes sporadically before settling at late times to a randomly chosen axis. See fig. 3 of Burrows et al. (2012) for a comparison. Note that, in a 2D simulation, the dipole axis is required to lie along the z-axis; this is not the case in a 3D simulation.

explosion energy (Burrows et al. 1995). The matter heated in the gain region is subsequently advected into the PNS, where it first reradiates a fraction of the acquired energy and then merges with the radiating PNS. It is only after the explosion commences that the deposited energy might be retained to contribute to the asymptotic explosion energy. However, even though explosive expansion leads to diminished cooling as the matter temperatures decrease, there continues to be some neutrino cooling. More importantly, the exploding matter expands against gravity, so that much of the

ongoing neutrino energy deposited is used to lift the matter out of the deep potential well. This explains why the neutrino heating rates even during explosion are larger than the accumulation rate of the supernova blast energy in the first seconds of the explosion phase. Recombination of the nucleons into nuclei will provide a boost ($\sim\!9$ MeV per baryon) to the asymptotic kinetic energy of the supernova ejecta, but the associated recombining mass is generally not large (here $\sim\!0.08~M_{\odot}$). Moreover, the associated total energy is comparable to the gravitational binding term. As a result, it ap-

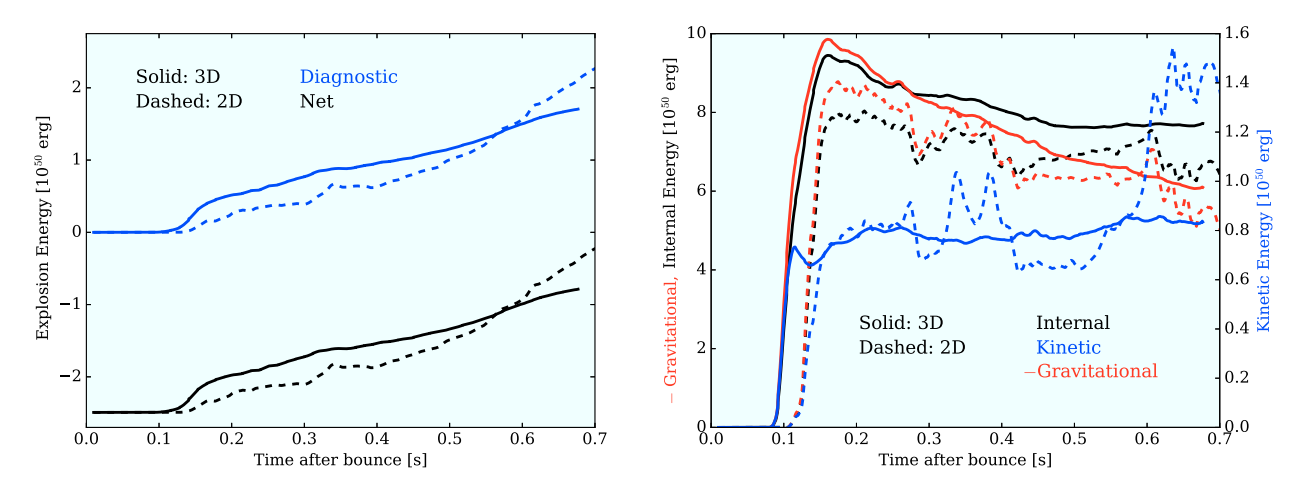


Figure 6. Left: Diagnostic (blue) and net (black) explosion energies (in 10^{50} erg) for the $16\,\mathrm{M}_\odot$ progenitor as a function of time after bounce (in seconds). Right: Internal (blue, left y-axis) and kinetic (green, right y-axis) energies (in 10^{50} erg) as a function of time after bounce (in seconds). Solid indicates the 3D model and dashed the corresponding 2D model for both figures. The diagnostic energy (left, green) does not account for the gravitational overburden of $\sim 2.5 \times 10^{50}$ erg exterior to our simulation grid (outer boundary $10\,000\,\mathrm{km}$). The total explosion energy (blue) is not yet positive for the 3D simulation (at 677 ms after bounce), though the 3D simulation explodes slightly earlier. The 3D simulation maintains a higher internal energy, by ~ 15 per cent, through the end of the simulation, and a higher explosion energy, but similar kinetic energies, until ~ 550 ms after bounce. The subsequent rise in explosion energy for the 2D model corresponds with the steep rise in its kinetic energy, also seen in Vartanyan et al. (2018) for the same $16\,\mathrm{M}_\odot$ progenitor, but with a different initial setup. Such a sharp rise in kinetic energy is not seen in our 3D simulation.

pears that the supernova will take many seconds to achieve its final energy. Therefore, even though our 3D simulation of this $16~M_{\odot}$ progenitor's core has been conducted farther post-bounce than any other simulation with state-of-the-art numerics and microphysics, we have captured only the early stages of an explosion that will need to be followed numerically for a few more seconds to witness the asymptoting of the explosion energy (Müller 2016; Müller et al. 2017).

The total energy we plot in Fig. 6 is comprised of the kinetic energy, the thermal energy, the recombination energy, and the gravitational energy of the ejecta. The so-called diagnostic energy ignores the binding energy (thermal plus gravitational) of the progenitor exterior to the computational domain. Here, the total energy quoted includes this penalty, different for every progenitor and outer computational boundary radius; including this term is required to assess the true supernova explosion energy.

We calculate diagnostic energies for our $16~M_{\odot}$ progenitor in 3D and 2D, summing the kinetic, thermal, gravitational, and nuclear binding energies interior to our $10\,000\,\mathrm{km}$ simulation grid where the matter parcel's Bernoulli term is positive. We correct for the gravitational binding energy of 2.5×10^{50} erg exterior to our grid, and plot both the diagnostic (blue) and net (black) explosion energies in the left-hand panel of Fig. 6. In the right-hand panel, we plot the thermal (blue, left *y*-axis), gravitational (red, left *y*-axis), and kinetic (green, right *y*-axis) energies (in 10^{50} erg) as a function of time after bounce (in seconds). Solid indicates the 3D model and dashed the 2D analogue for both figures.

The 3D model explodes slightly earlier and initially has a higher explosion energy than its 2D model counterpart (Fig. 6). At the end of the simulation, 677 ms after bounce, the 3D model has a diagnostic explosion energy of 1.7×10^{50} erg. Accounting for the gravitational overburden, the total explosion energy (blue) is not yet positive for the 3D simulation (-0.8×10^{50} erg). Before ~ 550 ms after bounce, the 3D simulation maintains similar kinetic energies and a higher internal energy by ~ 15 per cent than its 2D analogue. Thenabouts, the 2D model explosion energy overtakes that of the 3D model, with the rise in explosion energy corresponding to a

steep rise in its kinetic energy at a growth rate of $\sim \! 5 \times 10^{50}$ erg s $^{-1}$. Such a rise, also at $\sim \! 550$ ms after bounce, is seen in Vartanyan et al. (2018) for the same $16~M_{\odot}$ progenitor, but with a different initial setup. It is not seen in our 3D simulation. We conjecture that the stronger dipole and quadrupole moments of the 2D simulation (Fig. 4, right) relative to those of the corresponding 3D model at late times contribute to this divergence in kinetic energy. At the end of our simulation, the explosion energy for the 3D model is climbing at a rate of approximately 2.5×10^{50} erg s $^{-1}$, half that of the 2D case. Similar energy growth rates are found for the 3D simulations in the literature (see e.g. Müller et al. 2017) and necessitate continuing 3D simulations for several seconds.

In Fig. 7, top panel, we illustrate the heating rates and the gain mass as a function of time after bounce for the 3D (solid) and 2D (dashed) simulations of the 16 M_☉ progenitor. Just prior to explosion, at \sim 100 ms, the heating rate for the 3D simulation is \sim 30 per cent (2 Bethe s⁻¹) higher than for the corresponding 2D model. The gain mass is also slightly higher for the 3D model, exceeding 0.12 M_{\bigodot} at the end of our simulation). After ${\sim}150$ ms post-bounce, we see more variability in the heating rate for the 2D simulation than for the 3D simulation. Through almost \sim 700 ms after bounce, the growth rate of the explosion energy is less than 20 per cent of the heating rate, the difference due to the work done against gravity by the ejecta. It is not until late times that the growth rate of the explosion energy is expected to be close to the heating rate. In the middle panel, we show the spread of the inner boundary of the gain region a function of time after bounce, defined here where the net heating (heating minus cooling) is greater than 10 per cent of the heating alone. The 3D simulation (green, solid) maintains a much larger variation in radial boundary throughout the evolution, extending almost twice as far at late times as the 2D model. In the bottom panel, we show the heating efficiency η , defined as the heating rate divided by the luminosity entering the gain region,

$$\eta = \frac{Q_{\text{heat}}}{I_{\text{tot}} + I_{\text{D}}} \,. \tag{5}$$

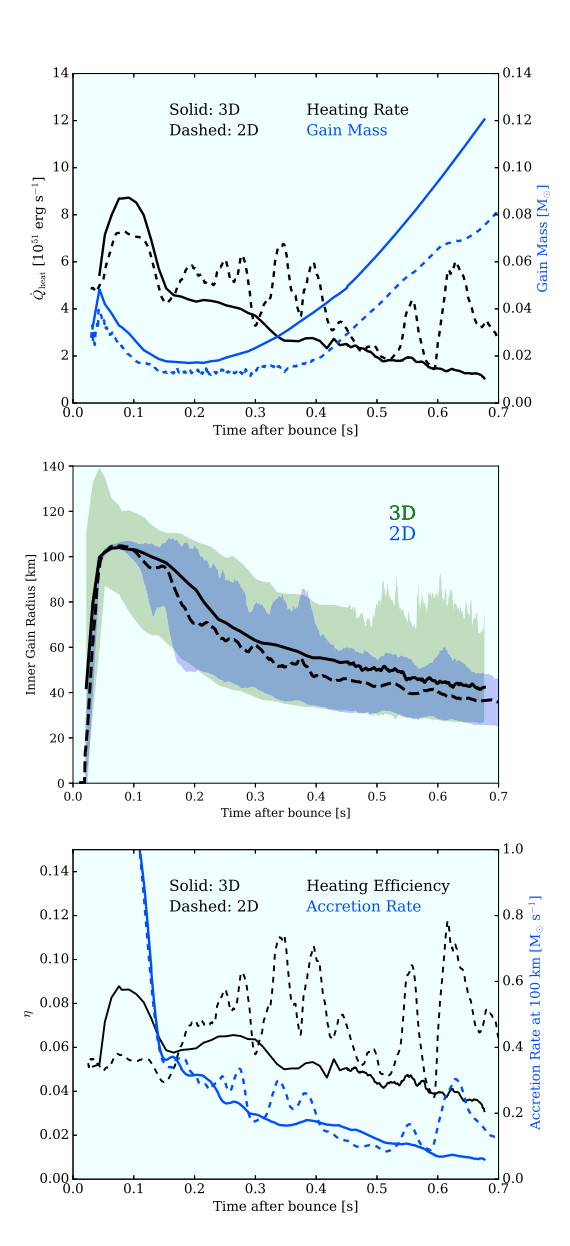


Figure 7. Top: We illustrate the heating rates (blue, 10^{51} erg s⁻¹), and the gain mass (black, in $10^{-3}~{\rm M}_{\odot}$) as a function of time after bounce (in seconds) for the 3D (solid) and 2D (dashed) simulations of the 16 M_{\top} progenitor. Prior to explosion (\sim 100 ms), the heating rate for the 3D simulation is \sim 30 per cent higher than for the 2D simulation. The gain mass is also slightly higher for the 3D model, exceeding 0.12 M_O at the end of our simulation. Middle: Inner boundary of the gain region (in km) as a function of time after bounce (in seconds). Black lines depict the mean positions of the inner gain region (solid for 3D, dashed for 2D). The 3D simulation (green, solid) maintains a much larger variation of the inner boundary of the gain region throughout the evolution. *Bottom*: Heating efficiency η (black), defined as the gain-region heating rate divided by the sum of the v_e and $\bar{\nu}_e$ luminosities entering the gain region, and the accretion rate at 150km (blue, in M_{\odot} s⁻¹). Through the first ~150 ms, the 3D simulation (green) has a heating efficiency \sim 40 per cent higher than the 2D (blue) simulation. However, after \sim 200 ms, the 2D simulation overtakes the 3D simulation, and showcases a high degree of variability over \sim 50 ms time-scales. Note the correlation between jumps in accretion rate and jumps in heating rates (and efficiencies) in the 2D simulation.

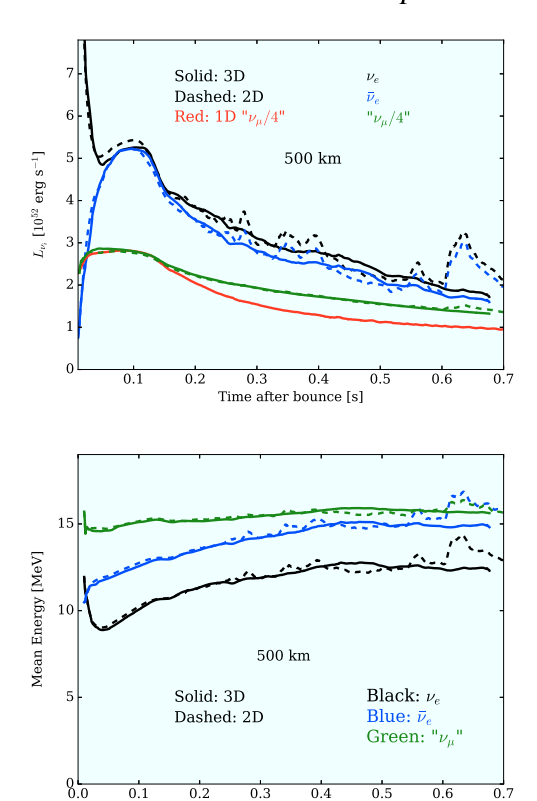


Figure 8. Neutrino luminosity (top, 10^{51} erg s⁻¹) and average neutrino energy (bottom, MeV) as a function of time after bounce (in seconds) at 500 km. Note that the luminosities and average energies for 2D and 3D are remarkably similar and show a significant difference only after 600 ms after bounce.

Through the first \sim 150 ms, the 3D simulation has a heating efficiency of \sim 0.09, 40 per cent higher than the corresponding 2D model. However, after 200 ms, the efficiency of the 2D simulation overtakes that of the 3D simulation, and showcases a high degree of variability with a time-scale of \sim 50 ms.

3.3 Luminosity and mean energies

In Fig. 8, we plot the luminosity (top) and mean energies (bottom) at a radius of 500 km as a function of time after bounce. Note that the luminosities and average energies for the 2D and 3D models are remarkably similar and show significant difference only beyond \sim 600 ms after bounce. We note, however, key differences in the electron–neutrino luminosities through the first \sim 150 ms, with the 2D simulation boasting a luminosity \sim 7 per cent larger than that for the 3D simulation. Furthermore, the 'heavy'-neutrino luminosity is \sim 3 per cent smaller for the 2D simulation than for the 3D simulation over the same time period. We explore this more in Section 3.5. Here, we remark that the interplay between the greater electron-neutrino luminosity and the smaller 'heavy' neutrino luminosity in the critical first 100 ms of our 2D simulation (compared to our 3D model) impede earlier explosion revival in the 2D case. The former strips the gain region of energy deposition by neutrinos (since the electron-type neutrinos have a much higher absorption opacity than the 'heavy'-type neutrinos). Furthermore, the greater 'heavy'-neutrino luminosity in the 3D simulation may act in the same direction as the axial-vector many-body correction to produce a harder electron-neutrino spectrum and facilitate explosion

360 D. Vartanyan et al.

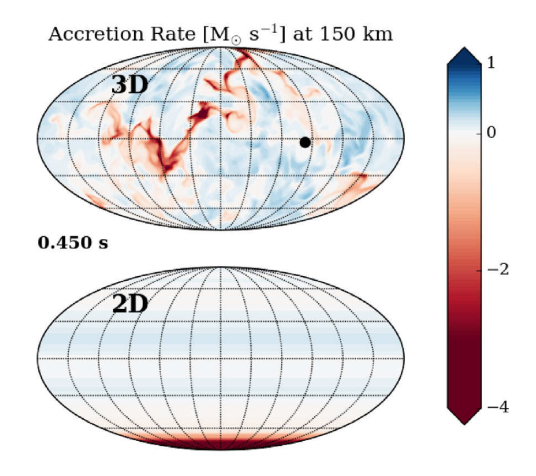


Figure 9. Mollweide projections of the accretion rate for the 3D and the 2D simulations at 450 ms after bounce. The spatial variation of accretion rate in the 3D simulation is in sharp contrast with the accretion rate in the 2D simulation, where we see only a dominant dipole component in the Southern hemisphere.

(Burrows et al. 2018). The culmination of these effects is visible in Fig. 7, top panel, where a small difference in the respective luminosities translates into a significantly smaller heating rate in the 2D simulation compared to the analogous 3D simulation. In Fig. 9, we show Mollweide projections of the accretion rate for the 3D and 2D models. The spatial variations for the 3D simulation for the accretion rate contrast sharply with that for the 2D simulation, in which we see a dominant dipole component only in the Southern hemisphere.

3.4 Ejecta composition

Our calculations follow the evolution in space and time of the electron fraction, Y_e . This quantity is an essential determinant of subsequent nucleosynthesis. While we do not in this paper derive the detailed elemental composition of our ejecta, the distributions of the entropies and Y_e s in the inner explosion debris provide qualitative information on the likely character of the emergent element burden. In our previous 2D simulations (Vartanyan et al. 2018), histograms of the ejecta Y_e were derived. What we found was that much of the ejecta have Y_e s above 0.5, implying that the ejected matter has been processed by differential v_e and \bar{v}_e absorption that has made some of it proton-rich. This is what we witness in this 3D simulation, though whether this is a generic outcome remains to be determined. Proton-rich ejecta could be a site of the p- and vpprocesses (Fröhlich et al. 2006; Pruet et al. 2006; Wanajo, Janka & Kubono 2011) and might be the context for the production of some of the first peak of the r-process (Hoffman et al. 1996; Fröhlich et al. 2006; Pruet et al. 2006; Wanajo et al. 2011; Bliss, Arcones & Qian 2018; Frebel 2018).

In Fig. 10, we provide a histogram of the ejecta mass distribution in Y_e at 0.529 s after bounce. The green bars indicate the results of the 3D simulation, and the blue bars that of the 2D simulation. Though both models peak at $Y_e = 0.5$, we find the interesting result that the ejecta distribution in the 2D model has a wider tail extending out to both higher (>0.55) and lower (<0.5) Y_e than the 3D simulation at any given time. For much of the evolution, the ejecta of the 3D simulation spans $Y_e \sim 0.5$ –0.55, whereas the ejecta in the 2D simulation encompasses $Y_e \sim 0.45$ –0.6. Only at late times

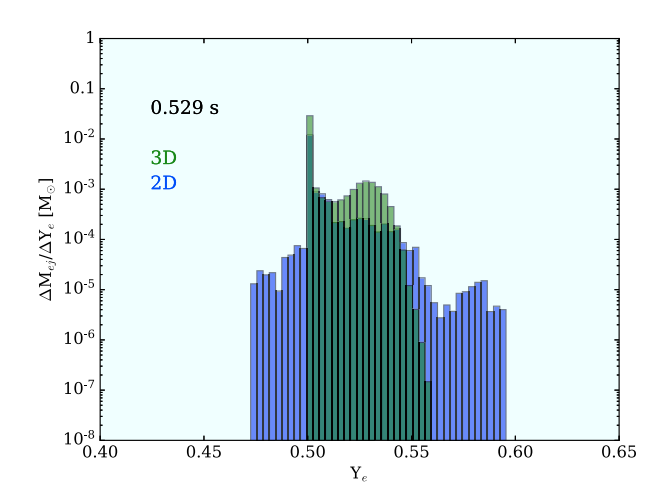


Figure 10. Histogram of ejecta mass distribution by Y_e at 0.529 s) after bounce. The green bars indicate the results of the 3D simulation, and the blue those for the 2D simulation. We find the interesting result that the ejecta mass distribution in 2D has a tail extending out to both higher (>0.55) and lower (<0.5) Y_e than the 3D simulation at a given time.

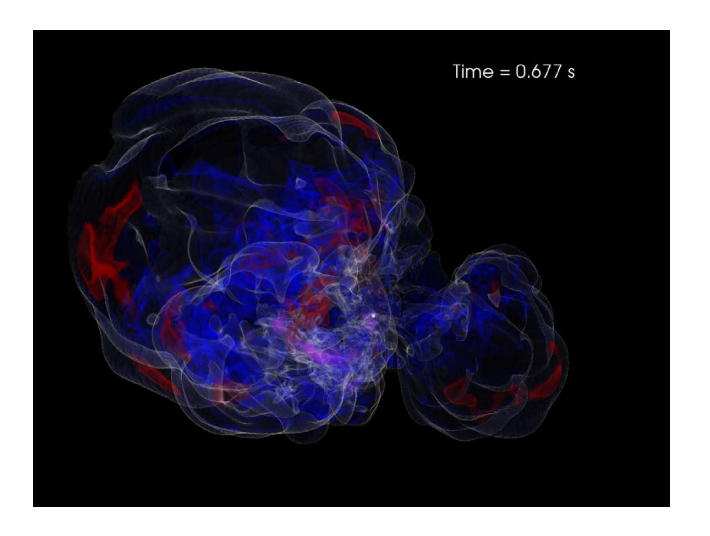


Figure 11. Y_e distribution at \sim 677 ms after bounce. The white 'veil' encompasses the expanding plumes, just interior to the shock radius, at a Y_e of 0.5. The blue plumes indicate a Y_e spanning the interval 0.5–0.52, and the red caps a Y_e greater than 0.52. The latter is concentrated along the exterior cusps of the plumes, and interior where accretion is funnelled on to the PNS. Note the resemblance of the high- Y_e distribution to the entropy distribution in Fig. 1. The violet tail shows the low- Y_e (<0.5) ejecta seen in Fig. 10. This trailing 'tail' is also visible in the density evolution of the progenitor.

does the 3D simulation have significant low- Y_e ejecta at large radii (see the violet tail in Fig. 11).²

In an earlier paper on 2D models (Vartanyan et al. 2018), we found that only the $16 \, \mathrm{M}_{\odot}$ progenitor had an ejecta- Y_e distribution that extended to lower Y_e , among the four progenitors considered. We claimed that an anisotropic explosion, with much of the outflow directed towards one hemisphere, would leave the opposite hemisphere with relatively untouched neutron-rich material. We see a

 2 We provide here the Y_e distribution in ejecta (defined as gravitationally unbound mass) beyond 1000 km. We also looked at the Y_e mass distribution of ejecta beyond 100 km. Our conclusion that our 3D simulation has a narrower Y_e span than the 2D model, remains unchanged.

similar result here. The 3D simulation, on the other hand, produces a more omnidirectional explosion — leaving little matter untouched. The achievement of higher Y_e in 2D can similarly be understood — the concentration of explosion in one direction in the 2D simulation allows ample neutrino processing of the ejecta to higher Y_e .

We illustrate the 3D distribution of Y_e in the ejecta in Fig. 11 at \sim 667 ms after bounce. The white 'veil' illustrates a Y_e of 0.5, just interior to the location of the shock radius. The high- Y_e plumes correspond to the high-entropy plumes of Fig. 1, with the blue plumes indicating Y_e 's that span 0.5–0.52, and the red blobs Y_e greater than 0.52. The latter is concentrated along the exterior cusps of the plumes, and in the interior where accretion is funnelled on to the PNS. Note the resemblance of the high- Y_e distribution in Fig. 11 to the entropy distribution in Fig. 1.

3.5 Inner PNS convection

The original delayed explosion mechanism of Wilson (1985) was facilitated by the enhancement of the driving neutrino luminosities by what he termed 'neutron-finger' convection. This was a doubly diffusive instability, akin to salt-finger convection in the oceans, that was suggested to result in an otherwise stably stratified PNS. A Ledoux-stable balance of Y_e and entropy gradients was thought to be undermined by the more rapid diffusion of energy vis à vis lepton number. Wilson captured this effect in 1D spherical models of explosion with a mixing-length-like diffusive flux, and the v_e and \bar{v}_e luminosities were thereby augmented by \sim 25 per cent. Without this effect, Wilson's models did not explode. However, Bruenn & Dineva (1996) showed that the core was not unstable to such 'neutron-finger' convection, and this was confirmed by Dessart et al. (2006) using 2D simulations. However, after bounce, there is a region in the PNS between \sim 10 and \sim 30 km that is in fact unstable to classical convection, driven mostly by negative Y_e gradients. This PNS convection is a feature in all modern multidimensional simulations of CCSN. In their study, Dessart et al. (2006) noticed that this overturning convection increased the emergent luminosities, but by the end of their simulation \sim 200–300 ms after bounce this increase was not large. In addition, inner PNS convection and the outer neutrino-driven convection interior to the stalled shock did not merge into one large convective zone. Given this, Dessart et al. (2006) concluded that PNS convection was not centrally important to the neutrino mechanism of CCSNe.

On the contrary, in their study of the lowest mass progenitor stars, Radice et al. (2017) found that the contribution of a PNS convection boost to the emergent neutrino luminosities grew with time after bounce, and could reach significant fractions. This was particularly true for $\bar{\nu}_e$ and ν_μ neutrinos, for which the respective neutrinospheres are deepest. Here, we explore the corresponding effects and numbers for our 3D simulation of the 16 M $_{\odot}$ progenitor of Woosley & Heger (2007), and compare them to the 2D case.

We plot in Fig. 12 the PNS mass (in M_{\odot} , blue) and mean radius (black) as a function of time after bounce for the 3D (solid), 2D (dashed), and 1D (red) simulations of the $16~M_{\odot}$ progenitor. The PNS surface here is defined where the density is $10^{11}~g\,cm^{-3}$. The baryonic PNS mass in our 3D simulation at \sim 677 ms after bounce is \sim 1.57 M_{\odot} (1.6 M_{\odot} in the 2D model, 1.63 M_{\odot} in the 1D model), corresponding to a gravitational mass of 1.42 M_{\odot} (1.44 M_{\odot} in the 2D model, 1.47 M_{\odot} in the 1D model). The PNS mass reflects the disruption of net accretion on to the PNS. Interestingly, we find that the difference between the PNS mass for the 1D and 2D models is roughly comparable to the difference in the same quantity between the 2D and the 3D models at late times, despite the absence of ex-

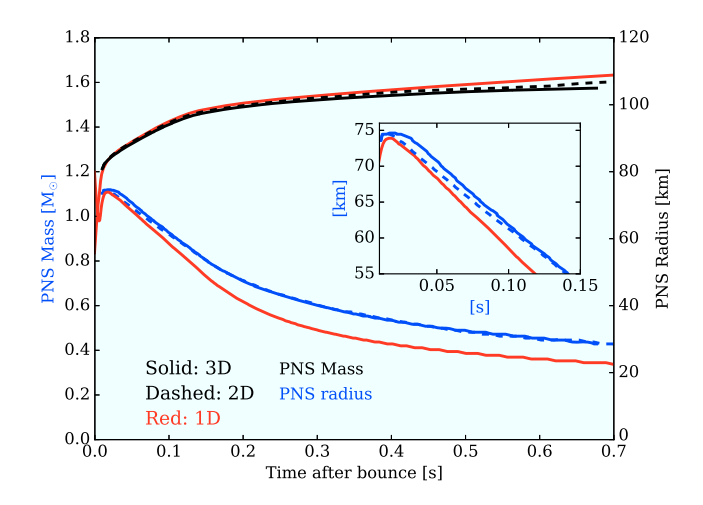


Figure 12. The PNS mass (in M_{\odot} , blue) and radius (in km, black) as a function of time after bounce (in seconds) for the 3D (solid), 2D (dashed), and 1D (red) simulations of the 16 M_{\odot} progenitor. At late times, the PNS radii for the 2D and 3D simulations are virtually identical, but significantly smaller in the 1D case. The larger PNS mass in 1D than 2D, and in 2D than 3D, is due to the longer accretion history than in 3D, where we see early explosion. In the inset, we show the PNS radius zoomed in for the first 150 ms after bounce. Until \sim 140 ms after bounce, the PNS radius in the 2D simulation is as much as \sim 3 per cent smaller than for the 3D simulation.

plosion in the 1D model and the correspondingly lengthier accretion history. Furthermore, at late times, the mean PNS radii in the 2D and 3D simulations are virtually identical (\sim 29 km) but are significantly smaller in the 1D case (\sim 23 km). A similar dependence of the PNS radii on simulation dimension was found in Radice et al. (2017) and Vartanyan et al. (2018). Here, we have the opportunity to compare such quantities to that of a 3D simulation. In the inset, we show the PNS radius zoomed-in for the first 150 ms after bounce. Until \sim 140 ms after bounce, the PNS radius in the 2D simulation is as much as \sim 3 per cent smaller than in the 3D model, lying between the PNS radii in the 3D simulation and in the 1D simulation. Simultaneously, as shown in Fig. 8, the 'heavy'-neutrino luminosity is slightly smaller in the 2D simulation than in the 3D simulation. At later times, both the 'heavy'-neutrino luminosity and the PNS radius in the 1D simulation are significantly lower than in the multidimensional simulations (see also Radice et al. 2018; Vartanyan et al. 2018). On time-scales greater than \sim 200 ms, PNS convection boosts the 'heavy'-neutrino luminosities in the 2D and 3D simulations. Furthermore, the shrinking PNS radius comes into close contact with the inner convective region after 200 ms (see Fig. 13), explaining the larger PNS radii in multidimensional simulations. However, electron-type neutrino luminosities are higher in 1D than in multidimensional simulations simply because that model does not explode, and accretion power remains significant.

In Fig. 13, we provide a space–time diagram of the standard deviation over angle of the radial velocity within the inner 100 km through 300 ms after bounce for the 3D (left) and 2D (right) models. Both convective regions are visible here as the bright regions — the interior convective band is similar to that seen in Dessart et al. (2006), and the exterior, neutrino-driven convection recedes to \sim 50 km by \sim 300 ms. The interior convective zone in the 2D simulation is a few kilometres wider and has higher convective velocities than its 3D counterpart. Furthermore, we see more variation in the radial location of the convective zones in the 2D simulation. However, in the 3D simulation, the exterior, neutrino-driven convective region is located deeper in at early times, reaching \sim 80 km

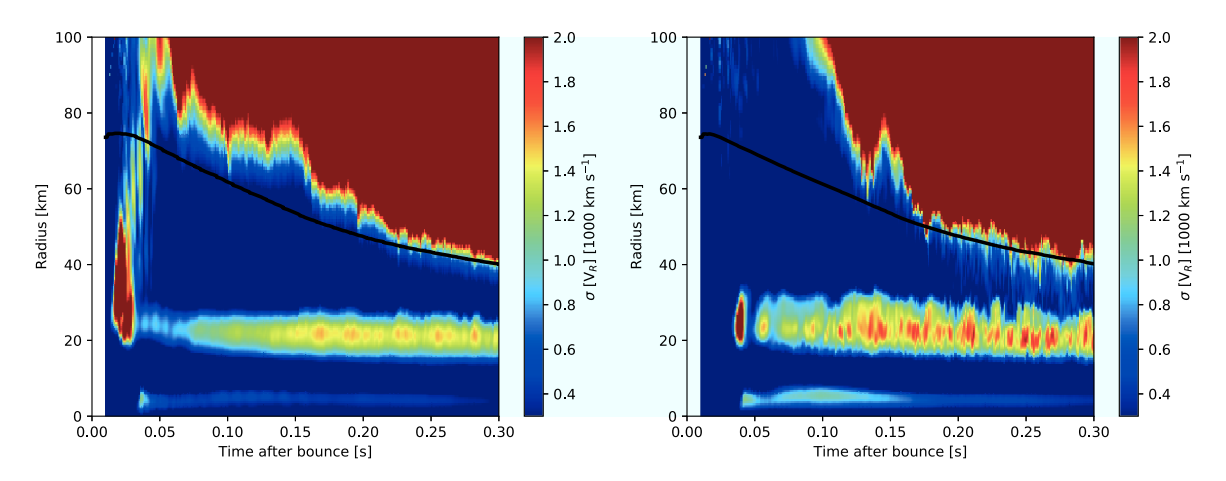


Figure 13. A space–time diagram of the standard deviation $\left(\sqrt{\langle(v_r-\langle v_r\rangle)^2\rangle}\right)$ over angle of the radial velocity within the inner 100km through 300 ms after bounce for the 3D (left) and 2D (right) models. Note that it is significantly smaller in 3D than in 2D (see also Fig. 14). Both the outer and inner (PNS) convective regions are visible here, and the interior convective zone is a band in velocity similar to that seen in Dessart et al. (2006). The black lines illustrate the mean PNS radius, which in 3D, and not 2D, is sampled by the outer neutrino-driven convection through the first 120 ms after-bounce. By \sim 300 ms after bounce, the exterior convective zone has receded to \sim 50 km. In the 2D simulation, the interior convective zone is a few km wider and has higher convective velocities by several hundred km s⁻¹ than its 3D counterpart. Furthermore, we see more variation in the radial location of the convective zones in the 2D simulation, with the outer convective zone making excursions almost to the inner convective zone by \sim 300 ms after bounce. See the text for further discussion.

by \sim 50 ms after bounce in the 3D simulation (by comparison, the exterior convective region in the 2D case reaches 80 km more than 100 ms after bounce). Through the first \sim 150 ms, this exterior convection reaches down into the PNS region in the 3D (but not the 2D) simulation. This may explain the slightly increased neutrino luminosities and shock radii in the 3D simulation seen in Figs 8 and 12 at these earlier times. Lastly, we see a turbulent 'teardrop' in the 3D simulation extending from \sim 20 to \sim 80 km in the first \sim 40 ms after bounce, trailing off to both the inner and outer convective regions by \sim 60 ms after bounce. By comparison, this feature is much smaller in extent and delayed to \sim 40 ms after bounce in the 2D model. The PNS convective zone has a characteristic size of \sim 10 km, a turnover time of \leq 10 ms, and convective velocities of \sim 1000 km s⁻¹. This is a manifestation of the stronger turbulence within 100 km at early times in the 3D simulation.

We explore the convective differences in the 2D and 3D simulations in Fig. 14. We show velocity vectors (white) on a Y_e colourmap depicted on an x-y slice of the 3D simulation (left) and an x-z slice of the 2D simulation (right) at \sim 57 (top), \sim 304 (middle), and \sim 667 (bottom) ms after bounce to illustrate the evolution of inner PNS convection. The vector lengths are scaled to velocity and made to saturate at 2000 km s⁻¹. Note the characteristic convective whorls forming within the first \sim 60 ms after bounce.

3.6 On the possible presence of the LESA and the SASI

The LESA was proposed in Tamborra et al. (2014) as a neutrino-hydrodynamical instability resulting in $v_e - \bar{v}_e$ asymmetry. In an earlier work (Vartanyan et al. 2018), we explored the possibility of LESA by examining the dipole harmonic component, a_{10} , of the net lepton number flux. In that paper, we concluded that, at least in 2D, the effect was negligible and speculated that the inference of LESA may be a consequence of the use of the ray-by-ray approximation to multidimensional neutrino transport.

We now extend our exploration of the possible presence of the LESA, using for the first time an exploding 3D model with full physical realism. In Fig. 15, we depict the monopole and dipole components of the lepton asymmetry $(F_{v_e} - F_{\bar{\nu}_e})$ as a function of

time after bounce at 500 km for both our 3D and 2D simulations. Here, we follow O'Connor & Couch (2018) and plot instead the dipole magnitude,

$$A_{\text{dipole}} = 3 \times \sqrt{\sum_{i=-1}^{1} a_{\text{I}i}^2},\tag{6}$$

using the normalization scheme of Burrows et al. (2012). The net effect is to increase the strength of the dipole term relative to the monopole term by a factor of \sim 1.73 ($3/\sqrt{3}$). We conclude that we do indeed find a LESA (see also O'Connor & Couch 2018) effect, and that (at least for these models) it is stronger in 3D than in 2D. However, the magnitude of the fluctuations in the lepton asymmetry is larger in 2D than in 3D. In addition, whereas Tamborra et al. (2014) find that the dipole term overtakes the monopole term as early as \sim 200 ms after bounce, we find that only after \sim 650 ms after bounce does the dipole component of the LESA become comparable to the monopole term. We continue to suggest that the ray-by-ray approach leads to a larger LESA, but this remains to be tested with a comparison of 3D ray-by-ray and multi-angle simulations.

We have also studied our 3D simulation for the possible presence of the SASI (Blondin et al. 2003) during any phase of its evolution. If present, this should manifest in a narrow and obvious frequency peak in various power spectra. Recent work in 3D (Walk et al. 2018) found pronounced peaks in the electron antineutrino power spectrum at \sim 60 and \sim 110 Hz that the authors associated with the SASI. In addition, Kuroda et al. (2016b, 2017) suggested that softer equations of state manifest the SASI, with its gravitational wave signature lasting for an interval of \sim 100 ms (a fraction of their simulation time) at frequencies of \sim 50–200 Hz. Fig. 16 portrays the Fourier decomposition of the dipole moment of the shock radius in both our 3D simulation and the associated 2D simulation out to 200 ms after bounce. We find no clear peak at these frequencies, either by this metric or in the gravitational wave emissions (not shown here). Moreover, a glance at Fig. 4 reiterates that we see in the 3D run no significant dipole term in the shock radius until

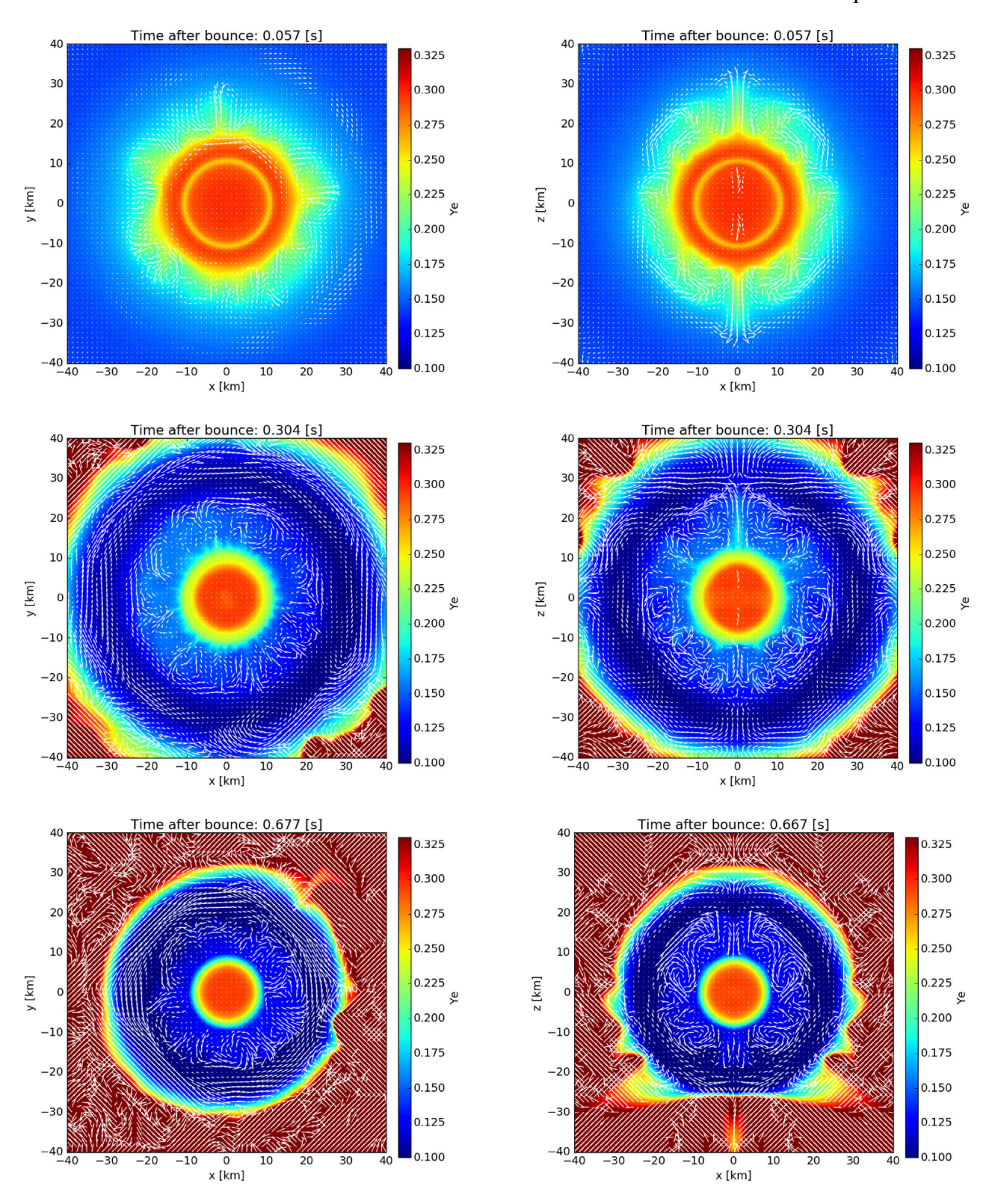


Figure 14. Velocity vectors (white) on a Y_e colourmap depicted on an x-y slice of the 3D simulation (left) and an x-z slice of the 2D simulation (right) at \sim 57 (top), \sim 304 (middle), and \sim 667 (bottom) ms after bounce to illustrate the evolution of inner-PNS convection. The velocity vector lengths are scaled to velocity and saturate at 2000 km s⁻¹. Note the characteristic convective whorls forming within the first \sim 60 ms after bounce. The region of inner convection (with $Y_e \sim$ 0.15–0.2) shrinks with the PNS, and at later times the exterior, neutrino-driven convective region (with $Y_e \gtrsim$ 0.3) is visible beyond \sim 30 km, with low- Y_e 'flares' traversing the boundary.

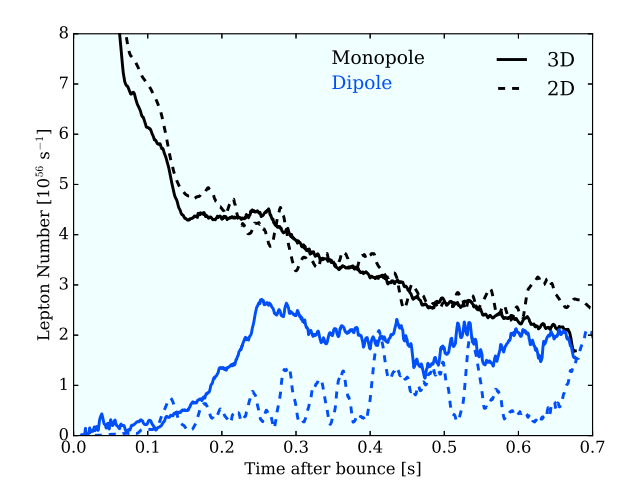


Figure 15. We plot the monopole (black) and dipole (blue) of net lepton number asymmetry F_{ν_e} – $F_{\bar{\nu}_e}$ (in units of 10^{56} s⁻¹) as a function of time after bounce (in seconds) at 500 km to explore the possible appearance of the 'LESA' phenomenon. Solid indicates the 3D model and dashed the 2D model. We do see the LESA effect, and the dipole term in the 3D simulation is larger and less variable than in the corresponding 2D model. However, the dipole term becomes comparable in magnitude to the monopole term only after \sim 650 ms.

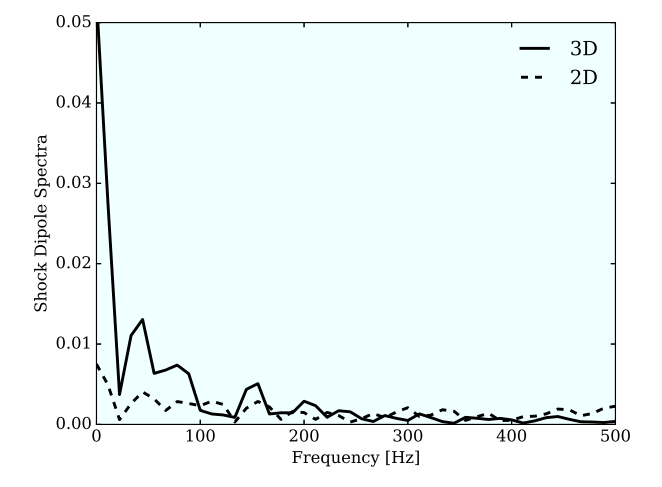


Figure 16. We plot the Fourier decomposition of the shock radius dipole component as a function of frequency (in Hz) for the first 100 ms after bounce for the 3D (dashed) and 2D (solid) simulations. Note that while the dipole component is insignificant for both models early on, it is larger for the 3D model during the first \sim 100 ms. This is also as seen in Fig. 4 (solid red line, right-hand panel).

after explosion.³ Therefore, we conclude that we have no evidence for the SASI in our $16~M_{\odot}$ simulations. However, since we find an early explosion in both the 3D and 2D simulations, perhaps the SASI may have had insufficient time to develop. It is important to note, however, that O'Connor & Couch (2018) likewise did not see a SASI for their 3D simulation (which was carried out to $\sim 600~m$ m after bounce, and did not explode) of a $20~M_{\odot}$ progenitor when incorporating velocity dependence. Note that the small bump at $\sim 40~Hz$ in Fig. 4 corresponds to small-amplitude oscillations of the shock dipole in the first $\sim 100~m$ s after bounce. This feature is

easily associated with the characteristic large-scale advective and convective time-scales in the region between the shock and the PNS.

We summarize here some of the catalysts to explosion in 3D. The $16\,M_\odot$ progenitor model (Woosley & Heger 2007) upon which we focus in this paper has a steep density dropoff interior to $1.7\,M_\odot$ due to its Si–O interface. Such a sharp density drop has been shown to facilitate explosion in models incorporating turbulence (be they 2D or 3D) (Vartanyan et al. 2018) and we witnessed the explosion of this model in our previous 2D study. In addition, our inclusion of the many-body effect on the neutrino–nucleon scattering cross-sections (Burrows et al. 2018) and the introduction of the significant velocity perturbations to the progenitor are both conducive to explosion. These aspects, in addition to the effects of GR and heating due to inelastic neutrino–electron and neutrino–nucleon scattering, seem to be some of the agents of 'success'.

4 CONCLUSIONS

We have presented in this paper one of the first non-rotating, stateof-the-art, full-microphysics simulations in three spatial dimensions to explode as a supernova. The explosion of a 16 M_☉ progenitor is fully underway by \sim 200 ms after bounce and at the end of the simulation is accumulating energy at a rate that if continued would reach \sim 0.5 Bethes (0.5 \times 10⁵¹ erg) within 2 s. However, what its final asymptotic energy will be remains to be seen. The gravitational mass of the remaining neutron star is \sim 1.42 M $_{\odot}$. The morphology of the emerging debris field has a roughly dipolar structure, with two asymmetric wide-angle lobes (one large, one small), whose axis emerged randomly. Whether slight rotation would impose an axis for the ejecta, or what rotation rate would be necessary to bias the emergent explosion axis, is not here determined. By the end of the simulation, an exploding debris field is accompanied by simultaneous inward accretion between the expanding lobes of some of the inner-progenitor matter, partly responsible for maintaining a driving neutrino luminosity (Burrows et al. 2007a). Interestingly, the majority of the ejecta of this supernova are proton-rich, with Y_e between 0.5 and 0.56. This will have interesting consequences for the associated nucleosynthesis, with the potential to explain in part the first r-process peak and p-process yields (Hoffman et al. 1996; Fröhlich et al. 2006; Pruet et al. 2006; Wanajo et al. 2011; Bliss et al. 2018; Frebel 2018).

It has been shown in the past that vigorous turbulent convection behind the temporarily stalled shock is essential to ignite an explosion for almost all anticipated progenitor structures. Only the rare progenitors at the lowest ZAMS masses with very steep density profiles exterior to the collapsing Chandrasekhar core explode in spherical symmetry (Kitaura, Janka & Hillebrandt 2006; Burrows, Dessart & Livne 2007c; Radice et al. 2018). The turbulent motions, boasting as they do a large effective ' γ ' connecting kinetic energy with pressure/stress, are one agency. Another is the consequently larger gain region in the multi-D turbulent context. A third could be the longer dwell times in the gain region occasioned by the non-radial motions (Murphy & Burrows 2008). Aside from the necessity in most cases of the turbulence enabled in the multi-D context, the specific progenitor density profile is a major determinant, though the dependence upon the associated 'compactness' parameter (O'Connor & Ott 2013) of the 'explodability' of a model is non-monotonic in subtle ways (Burrows et al. 2018). Models with the lowest compactness may explode even in 1D via a wind mechanism (Burrows 1987). However, models with slightly higher compactness have trouble exploding (O'Connor et al. 2017; Burrows et al. 2018), while models with even higher compactness

 $^{^3}$ However, the dipole term is slighter stronger in the first \sim 100 ms for the 3D simulation than for its 2D counterpart.

(such as the $16\,M_\odot$ of this paper) explode rather easily. Clearly, the explodability's dependence upon progenitor density profile is not straightforward.

One aspect of this nuanced behaviour is the role of the accretion through the shock of the Si-O interface (see Summa et al. 2018; Vartanyan et al. 2018). The jump up in entropy at that interface is accompanied by a corresponding drop in mass density. If that drop is large and sharp, then when that interface is accreted through the stalled shock the confining ram pressure temporarily and abruptly declines, while not immediately altering the driving neutrino luminosities (emanating from the core) and heating rates. The consequence is often (as in the case studied in this paper) a kick into explosion, which in the immediate term is generally irreversible due to the quick diminution of neutrino cooling occasioned by expansion and the maintenance of heating. However, the magnitude and radius of this interface and the overall density profile of the core at collapse are functions of stellar evolution (and stellar progenitor models), emphasizing the centrality to the viability and character of CCSN explosion phenomenology of these initial states.

Another progenitor determinant of explosion may be its initial seed perturbations. It has been shown (Couch & Ott 2013, 2015; Müller & Janka 2015; Müller 2016; Burrows et al. 2018) that if the seeds are of sufficient strength, then the ability of turbulence to ignite explosion is enhanced. In the simulation highlighted in this paper, we imposed a modest physical perturbation to the accreted velocity field that may have helped or accelerated explosion. However, whether perturbations are important, or merely facilitators, has not been determined and the next generation of fully 3D progenitor models may illuminate this question (Couch et al. 2015; Müller et al. 2016).

Those realistic physical processes that were conducive to the 3D explosion we witnessed in this paper include neutrino-driven turbulence (Herant et al. 1994; Burrows et al. 1995), the net effects of GR (Bruenn, De Nisco & Mezzacappa 2001), the inclusion of inelastic scattering and energy redistribution via neutrino-electron and neutrino-nucleon scattering (Burrows et al. 2018; Just et al. 2018; Vartanyan et al. 2018), the many-body correction to neutrino nucleon scattering (Burrows & Sawyer 1998; Horowitz et al. 2017; Burrows et al. 2018), the accretion of a sharp Si-O interface at a propitious time (Vartanyan et al. 2018), and the imposition of velocity perturbations in the progenitor. A major consequence of the many-body correction is the decrease in the scattering rate that increases the neutrino emission rates. This is particularly true for the v_u s, and the resulting acceleration of core contraction leads to, among other things, the increase in the temperatures around the v_e and \bar{v}_e neutrinospheres. This leads to a slight hardening of the emergent v_e and \bar{v}_e spectra and an increase in the heating rate due to charged-current absorption on the free nucleons in the gain region. One of the most important future classes of investigations of direct relevance to the CCSN mechanism is the magnitude and role of many-body corrections to both the neutral-current and the charged-current (Burrows & Sawyer 1999; Roberts, Reddy & Shen 2012; Roberts & Reddy 2017) neutrino–matter interaction rates. We note as well that even though the number of viable published nuclear equations of state is dwindling, the EOS dependence of the outcome of collapse has not been definitively addressed, nor well explained. This will be a necessity in the years to come as laboratory constraints become ever more stringent.

While the results presented in this paper are quite encouraging, there remain a number of important caveats. Important among these are the dependence upon the spatial and energy-group resolutions.

In 3D, a resolution study, even with modern codes such as FORNAX, is expensive, but will be necessary to determine both the quantitative and qualitative limitations of what we have presented here. The chaotic character of turbulent flow will make this a challenging endeavour for the community going forward. Moreover, we have conducted these calculations including the effects of GR in approximate fashion (Appendix A). Doing these calculations with full GR will be important and attempts in this direction have already been made (Roberts et al. 2016; Kuroda et al. 2018; Ott et al. 2018). To enable these forefront simulations, we still had to make approximations in the neutrino sector. Foremost among these is the use of the moment formalism and an analytic closure for the second and third moments. While recent tests of the accuracy of such an approach in the core-collapse context are encouraging (Richers et al. 2017; O'Connor et al. 2018), solving the full Boltzmann equation with neutrino angles in the full six-dimensional phase space will require a significantly more capable national and international computational infrastructure. Finally, it has been shown that explodability when near criticality and in multi-D is a sensitive function of details in the neutrino-matter interaction rates (Burrows et al. 2018) in a way not seen in 1D simulations. This puts a premium on implementing correctly the correct microphysics. All modellers aspire to this goal, but whether we or others actually have achieved this is, or should be, a constant worry.

The model we presented was non-rotating. We think that most collapsing cores, while they are certainly rotating, are not generically rotating at rates sufficient to make a qualitative difference most of the time (Emmering & Chevalier 1989; Faucher-Giguère & Kaspi 2006; Popov & Turolla 2012; Noutsos et al. 2013). However, this remains to be exhaustively explored. Rapid rotation can certainly affect the outcome, both directly and by providing significant free energy to feed large magnetic fields and enable the direct effects of magnetic stress, when strong, on the explosion dynamics (see e.g. Burrows et al. 2007b; Mösta et al. 2015). In fact, rapid rotation alone can affect the dynamics and facilitate explosion even when the expected magnetic field amplifications are ignored (Fryer & Warren 2002, 2004; Marek & Janka 2009; Summa et al. 2018). Moreover, rapid rotation can also generate a non-axisymmetric spiral-arm mode, which resembles the SASI in the rotating context and might enlarge the gain region and, thereby, facilitate explosion (Takiwaki et al. 2016; Summa et al. 2018). Curiously, if the explosion is suitably delayed, such a mode may also grow in the non-rotating context (Blondin & Shaw 2007; Rantsiou et al. 2011; Guilet & Fernández 2014; O'Connor & Couch 2018). This and other related issues are fruitful topics for future work.

However, we view the achievement of a 3D simulation that leads naturally to explosion, with competitive resolution, including all the relevant microphysics, using a state-of-the-art simulation tool, and calculating significantly post-bounce as a major milestone in the decades-long quest to resolve the CCSN puzzle in quantitative detail. What remains in the near term is to determine the progenitor mass dependence of the outcome of collapse in 3D, to understand the possible roles of rotation, to explain the supernova energies and neutron star masses observed, and to explain the morphologies of the debris fields seen in SNRs. Furthermore, a major motivation of all supernova simulations is the detailed explanation of the explosive production of the elements. The ejecta we find are mostly protonrich, and this emerges naturally from the detailed simulations. What the consequences are of this finding will be one of the topics of our future studies as we continue our quest to understand one of the most persistent problems in stellar and nuclear astrophysics.

ACKNOWLEDGEMENTS

The authors acknowledge helpful discussions with Todd Thompson regarding inelastic scattering, Evan O'Connor regarding the EOS, and Gabriel Martínez-Pinedo concerning electron capture on heavy nuclei. We also acknowledge invaluable support from Viktoriya Morozova with visualization using VisIt, and Sydney Andrews for helpful discussion and feedback. We acknowledge support from the U.S. Department of Energy Office of Science and the Office of Advanced Scientific Computing Research via the Scientific Discovery through Advanced Computing (SciDAC4) program and Grant DE-SC0018297 (subaward 00009650). In addition, we gratefully acknowledge support from the U.S. NSF under Grants AST-1714267 and PHY-1144374 [the latter via the Max-Planck/Princeton Center (MPPC) for Plasma Physics]. DR acknowledges partial support as a Frank and Peggy Taplin Fellow at the Institute for Advanced Study. The authors employed computational resources provided by the TIGRESS high performance computer centre at Princeton University, which is jointly supported by the Princeton Institute for Computational Science and Engineering (PICSciE) and the Princeton University Office of Information Technology, and by the National Energy Research Scientific Computing Center (NERSC), which is supported by the Office of Science of the U.S. Department of Energy (DOE) under contract DE-AC03-76SF00098. The authors express their gratitude to Ted Barnes of the DOE Office of Nuclear Physics for facilitating their use of NERSC. This overall research project is also part of the Blue Waters sustained-petascale computing project, which is supported by the National Science Foundation (awards OCI-0725070 and ACI-1238993) and the state of Illinois. Blue Waters is a joint effort of the University of Illinois at Urbana-Champaign and its National Center for Supercomputing Applications. This general project is also part of the 'Three-Dimensional Simulations of Core-Collapse Supernovae' PRAC allocation support by the National Science Foundation (under award #OAC-1809073). Under the local award #TG-AST170045, our ongoing supernova efforts are enhanced through access to the resource Stampede2 in the Extreme Science and Engineering Discovery Environment (XSEDE), which is supported by National Science Foundation grant number ACI-1548562. This work was performed under the auspices of the U.S. Department of Energy by Lawrence Livermore National Laboratory under Contract DE-AC52-07NA27344 and has been assigned an LLNL document release number LLNL-JRNL-757405. This work was performed under the auspices of the U.S. Department of Energy by Los Alamos National Laboratory under Contract DE-AC52-06NA25396 and has been assigned an LANL document release number LA-UR-18-28730. JD acknowledges support from the Laboratory Directed Research and Development program at Los Alamos National Laboratory.

REFERENCES

Ahmed Z. et al., 2012, Phys. Rev. Lett., 108, 102001

Bliss J., Arcones A., Qian Y.-Z., 2018, preprint (arXiv:1804.03947)

Blondin J. M., Shaw S., 2007, ApJ, 656, 366

Blondin J. M., Mezzacappa A., DeMarino C., 2003, ApJ, 584, 971

Bruenn S. W., 1985, ApJS, 58, 771

Bruenn S. W., Dineva T., 1996, ApJ, 458, L71

Bruenn S. W., De Nisco K. R., Mezzacappa A., 2001, ApJ, 560, 326

Burrows A., 1987, ApJ, 318, L57

Burrows A., 2013, Rev. Mod. Phys., 85, 245

Burrows A., Goshy J., 1993, ApJ, 416, L75

Burrows A., Sawyer R. F., 1998, Phys. Rev. C, 58, 554

Burrows A., Sawyer R. F., 1999, Phys. Rev. C, 59, 510

Burrows A., Thompson T. A., 2004, in Fryer C. L., ed., Astrophysics and Space Science Library, Vol. 302, Stellar Collapse. Kluwer, Dordrecht, p. 133

Burrows A., Hayes J., Fryxell B. A., 1995, ApJ, 450, 830

Burrows A., Reddy S., Thompson T. A., 2006, Nucl. Phys.s A, 777, 356

Burrows A., Livne E., Dessart L., Ott C. D., Murphy J., 2007a, ApJ, 655, 416

Burrows A., Dessart L., Livne E., Ott C. D., Murphy J., 2007b, ApJ, 664, 416

Burrows A., Dessart L., Livne E., 2007c, in Immler S., Weiler K., McCray R., eds, AIP Conf. Ser. Vol. 937, Supernova 1987A: 20 Years After: Supernovae and Gamma-Ray Bursters. Am. Inst. Phys., New York, p. 370

Burrows A., Dolence J. C., Murphy J. W., 2012, ApJ, 759, 5

Burrows A., Vartanyan D., Dolence J. C., Skinner M. A., Radice D., 2018, Space Sci. Rev., 214, 33

Colgate S. A., White R. H., 1966, ApJ, 143, 626

Couch S. M., O'Connor E. P., 2014, ApJ, 785, 123

Couch S. M., Ott C. D., 2013, ApJ, 778, L7

Couch S. M., Ott C. D., 2015, ApJ, 799, 5

Couch S. M., Chatzopoulos E., Amett W. D., Timmes F. X., 2015, ApJ, 808, L21

Dessart L., Burrows A., Livne E., Ott C. D., 2006, ApJ, 645, 534

Dolence J. C., Burrows A., Murphy J. W., Nordhaus J., 2013, ApJ, 765, 110

Emmering R. T., Chevalier R. A., 1989, ApJ, 345, 931

Faucher-Giguère C.-A., Kaspi V. M., 2006, ApJ, 643, 332

Frebel A., 2018, preprint (arXiv:1806.08955)

Fröhlich C., Martínez-Pinedo G., Liebendörfer M., Thielemann F.-K., Bravo E., Hix W. R., Langanke K., Zinner N. T., 2006, Phys. Rev. Lett., 96, 142502

Fryer C. L., Warren M. S., 2002, ApJ, 574, L65

Fryer C. L., Warren M. S., 2004, ApJ, 601, 391

Green J. et al., 2017, Phys. Rev. D, 95, 114502

Guilet J., Fernández R., 2014, MNRAS, 441, 2782

Hanke F., Marek A., Müller B., Janka H.-T., 2012, ApJ, 755, 138

Hanke F., Müller B., Wongwathanarat A., Marek A., Janka H.-T., 2013, ApJ, 770, 66

Heger A., Woosley S. E., Spruit H. C., 2005, ApJ, 626, 350

Herant M., Benz W., Hix W. R., Fryer C. L., Colgate S. A., 1994, ApJ, 435, 339

Hoffman R. D., Woosley S. E., Fuller G. M., Meyer B. S., 1996, ApJ, 460,

Horowitz C. J., 2002, Phys. Rev. D, 65, 043001

Horowitz C. J., Caballero O. L., Lin Z., O'Connor E., Schwenk A., 2017, Phys. Rev. C, 95, 025801

Janka H.-T., 2012, Annu. Rev. Nucl. Part. Sci., 62, 407

Janka H.-T., Melson T., Summa A., 2016, Annu. Rev. Nucl. Part. Sci., 66, 341

Juodagalvis A., Langanke K., Hix W. R., Martínez-Pinedo G., Sampaio J. M., 2010, Nucl. Phys. A, 848, 454

Just O., Bollig R., Janka H.-T., Obergaulinger M., Glas R., Nagataki S., 2018, preprint (arXiv:1805.03953)

Kitaura F. S., Janka H.-T., Hillebrandt W., 2006, A&A, 450, 345

Kuroda T., Takiwaki T., Kotake K., 2016a, ApJS, 222, 20

Kuroda T., Kotake K., Takiwaki T., 2016b, ApJ, 829, L14

Kuroda T., Kotake K., Hayama K., Takiwaki T., 2017, ApJ, 851, 62

Kuroda T., Kotake K., Takiwaki T., Thielemann F.-K., 2018, MNRAS, 477, L80

Lattimer J. M., Swesty F., 1991, Nucl. Phys. A, 535, 331

Lentz E. J. et al., 2015, ApJ, 807, L31

Liebendörfer M., Whitehouse S. C., Fischer T., 2009, ApJ, 698, 1174

Marek A., Janka H.-T., 2009, ApJ, 694, 664

Marek A., Dimmelmeier H., Janka H.-T., Müller E., Buras R., 2006, A&A,

Melson T., Janka H.-T., Marek A., 2015a, ApJ, 801, L24

Melson T., Janka H.-T., Bollig R., Hanke F., Marek A., Müller B., 2015b, ApJ, 808, L42

- Morozova V., Radice D., Burrows A., Vartanyan D., 2018, preprint(arXiv: 1801.01914)
- Mösta P., Ott C. D., Radice D., Roberts L. F., Schnetter E., Haas R., 2015, Nature, 528, 376
- Müller B., 2015, MNRAS, 453, 287
- Müller B., 2016, PASA, 33, e048
- Müller B., Janka H.-T., 2015, MNRAS, 448, 2141
- Müller B., Viallet M., Heger A., Janka H.-T., 2016, ApJ, 833, 124
- Müller B., Melson T., Heger A., Janka H.-T., 2017, MNRAS, 472, 491
- Murphy J. W., Burrows A., 2008, ApJ, 688, 1159
- Nordhaus J., Burrows A., Almgren A., Bell J., 2010, ApJ, 720, 694
- Noutsos A., Schnitzeler D. H. F. M., Keane E. F., Kramer M., Johnston S., 2013, MNRAS, 430, 2281
- O'Connor E., Couch S., 2018, ApJ, 865, 81
- O'Connor E., Ott C. D., 2013, ApJ, 762, 126
- O'Connor E., Horowitz C. J., Lin Z., Couch S., 2017, in Marcowith A., Renaud M., Dubner G., Ray A., Bykov A., eds, IAU Symp. Vol. 331, Supernova 1987A:30 years later – Cosmic Rays and Nuclei from Supernovae and their Aftermaths. p. 107
- O'Connor E., et al., 2018, J. Phys. G: Nucl. Part. Phys., 45, 104001
- Ott C. D., Roberts L. F., da Silva Schneider A., Fedrow J. M., Haas R., Schnetter E., 2018, ApJ, 855, L3
- Popov S. B., Turolla R., 2012, Ap&SS, 341, 457
- Pruet J., Hoffman R. D., Woosley S. E., Janka H.-T., Buras R., 2006, ApJ, 644, 1028
- Radice D., Burrows A., Vartanyan D., Skinner M. A., Dolence J. C., 2017, ApJ, 850, 43
- Radice D., Abdikamalov E., Ott C. D., Mösta P., Couch S. M., Roberts L. F., 2018, J. Phys. G: Nucl. Part. Phys., 45, 053003
- Rampp M., Janka H.-T., 2002, A&A, 396, 361
- Rantsiou E., Burrows A., Nordhaus J., Almgren A., 2011, ApJ, 732, 57
- Reddy S., Prakash M., Lattimer J. M., Pons J. A., 1999, Phys. Rev. C, 59, 2888
- Richers S., Nagakura H., Ott C. D., Dolence J., Sumiyoshi K., Yamada S., 2017, ApJ, 847, 133
- Roberts L. F., Reddy S., 2017, Phys. Rev. C, 95, 045807

- Roberts L. F., Reddy S., Shen G., 2012, Phys. Rev. C, 86, 065803
- Roberts L. F., Ott C. D., Haas R., O'Connor E. P., Diener P., Schnetter E., 2016, ApJ, 831, 98
- Seadrow S., Burrows A., Vartanyan D., Radice D., Skinner M. A., 2018, MNRAS, 480, 4710
- Shibata M., Kiuchi K., Sekiguchi Y., Suwa Y., 2011, Prog. Theor. Phys., 125, 1255
- Skinner M. A., Burrows A., Dolence J. C., 2016, ApJ, 831, 81
- Skinner M. A., Dolence J. C., Burrows A., Radice D., Vartanyan D., 2018, (arXiv:1806.07390)
- Steiner A. W., Hempel M., Fischer T., 2013, ApJ, 774, 17
- Sukhbold T., Woosley S. E., Heger A., 2018, ApJ, 860, 93
- Summa A., Janka H.-T., Melson T., Marek A., 2018, ApJ, 852, 28
- Takiwaki T., Kotake K., Suwa Y., 2012, ApJ, 749, 98
- Takiwaki T., Kotake K., Suwa Y., 2016, MNRAS, 461, L112
- Tamborra I., Hanke F., Janka H.-T., Müller B., Raffelt G. G., Marek A., 2014, ApJ, 792, 96
- Tews I., Lattimer J. M., Ohnishi A., Kolomeitsev E. E., 2017, ApJ, 848, 105 Thompson T. A., Burrows A., Horvath J. E., 2000, Phys. Rev. C, 62, 035802
- Thompson T. A., Burrows A., Pinto P. A., 2003, ApJ, 592, 434
- Vartanyan D., Burrows A., Radice D., Skinner M. A., Dolence J., 2018, MNRAS, 477, 3091
- Vaytet N. M. H., Audit E., Dubroca B., Delahaye F., 2011, J. Quant. Spec. Radiat. Transf., 112, 1323
- Walk L., Tamborra I., Janka H.-T., Summa A., 2018, preprint (arXiv:1807.02366)
- Wallace J., Burrows A., Dolence J. C., 2016, ApJ, 817, 182
- Wanajo S., Janka H.-T., Kubono S., 2011, ApJ, 729, 46
- Willingale R., Bleeker J. A. M., van der Heyden K. J., Kaastra J. S., 2003, A&A, 398, 1021
- Wilson J. R., 1985, in Centrella J. M., Leblanc J. M., Bowers R. L., eds, Numerical Astrophysics. Jones and Bartlett Publ., Boston, p. 422
- Woosley S. E., Heger A., 2007, Phys. Rep., 442, 269
- Woosley S. E., Weaver T. A., 1995, ApJS, 101, 181
- Woosley S. E., Heger A., Weaver T. A., 2002, Rev. Mod. Phys., 74, 1015

APPENDIX A: APPROXIMATE GENERAL RELATIVISTIC FORMULATION

As stated in Section 1, we use the M1 closure to truncate the radiation moment hierarchy by specifying the second and third moments as algebraic functions in terms of the zeroth and first. The basic equations of radiative transfer in the comoving frame that we solve are the zeroth- and first-moment equations of the full equation of radiative transfer for the specific intensity. For neutrino transfer, we currently follow the evolution of ν_e , $\bar{\nu}_e$, and ν_x neutrinos, where the latter represents the ν_μ , $\bar{\nu}_\mu$, and ν_τ , neutrinos collectively. With explicit neutrino source and sink terms, the full set of Newtonian radiation/hydrodynamic equations, with a specific focus on the neutrino radiation implementation relevant to the study of CCSNe, are

$$\rho_t + (\rho \mathbf{v}^i)_{i} = 0, \tag{A1}$$

$$(\rho \mathbf{v}_j)_{,t} + (\rho \mathbf{v}^i \mathbf{v}_j + P\delta^i_j)_{;i} = -\rho \phi_{,j} + c^{-1} \sum_{s} \int_0^\infty (\kappa_{s\varepsilon} + \sigma^{tr}_{s\varepsilon}) \mathbf{F}_{s\varepsilon j} d\varepsilon,$$
(A2)

$$\left[\rho\left(e + \frac{1}{2}\|\boldsymbol{v}\|^{2}\right)\right]_{t} + \left[\rho\boldsymbol{v}^{i}\left(e + \frac{1}{2}\|\boldsymbol{v}\|^{2} + \frac{P}{\rho}\right)\right]_{i} = -\rho\boldsymbol{v}^{i}\phi_{,i} - \sum_{s}\int_{0}^{\infty}\left(j_{s\varepsilon} - c\kappa_{s\varepsilon}E_{s\varepsilon} - \frac{v^{i}}{c}(\kappa_{s\varepsilon} + \sigma_{s\varepsilon}^{tr})\boldsymbol{F}_{s\varepsilon i}\right)d\varepsilon, \tag{A3}$$

$$(\rho Y_e)_{,t} + (\rho Y_e v^i)_{;i} = \sum_s \int_0^\infty \xi_{s\varepsilon} (j_{s\varepsilon} - c\kappa_{s\varepsilon} E_{s\varepsilon}) d\varepsilon, \tag{A4}$$

$$E_{s\varepsilon,t} + (F_{s\varepsilon}^i + v^i E_{s\varepsilon})_{;i} - v_{;j}^i \frac{\partial}{\partial \ln \varepsilon} P_{s\varepsilon i}^j = j_{s\varepsilon} - c\kappa_{s\varepsilon} E_{s\varepsilon}, \tag{A5}$$

$$\boldsymbol{F}_{s\varepsilon j,t} + (c^2 \boldsymbol{P}_{s\varepsilon j}^i + \boldsymbol{v}^i \boldsymbol{F}_{s\varepsilon j})_{;i} + \boldsymbol{v}_{;j}^i \boldsymbol{F}_{s\varepsilon i} - \boldsymbol{v}_{;t}^i \frac{\partial}{\partial \varepsilon} (\varepsilon \boldsymbol{Q}_{s\varepsilon ji}^k) = -c(\kappa_{s\varepsilon} + \sigma_{s\varepsilon}^{tt}) \boldsymbol{F}_{s\varepsilon j}, \tag{A6}$$

where e is the specific internal energy, $P = P(\rho, e, Y_e)$ is the pressure, ρ is the mass density, Y_e is the electron fraction, \mathbf{v}_i are the velocity components, κ_{se} and σ_{se}^{tr} are the absorption and transport scattering opacities, and $s \in \{\nu_e, \bar{\nu}_e, \nu_x\}$, where

$$\xi_{s\varepsilon} = \begin{cases} -(N_A \varepsilon)^{-1} & s = \nu_e, \\ (N_A \varepsilon)^{-1} & s = \bar{\nu}_e, \\ 0 & s = \nu_x. \end{cases}$$
(A7)

The corresponding radiation energy and momentum equations modified to approximately incorporate general relativistic effects are

$$E_{s\varepsilon,t} + (\alpha F_{s\varepsilon}^i + \mathbf{v}^i E_{s\varepsilon})_{;i} - \alpha \mathbf{v}_{;j}^i \frac{\partial}{\partial \ln \varepsilon} P_{s\varepsilon i}^j = \alpha (j_{s\varepsilon} - c\kappa_{s\varepsilon} E_{s\varepsilon}) + \alpha G^e,$$
(A8)

$$\boldsymbol{F}_{s\varepsilon j,t} + (c^2 \alpha \boldsymbol{P}_{s\varepsilon j}^i + \boldsymbol{v}^i \boldsymbol{F}_{s\varepsilon j})_{;i} + \alpha \boldsymbol{v}_{;j}^i \boldsymbol{F}_{s\varepsilon i} - \alpha v_{;k}^i \frac{\partial}{\partial c} (\varepsilon \boldsymbol{Q}_{s\varepsilon ji}^k) = -c\alpha (\kappa_{s\varepsilon} + \sigma_{s\varepsilon}^{tr}) \boldsymbol{F}_{s\varepsilon j} + \alpha \boldsymbol{G}_j^m, \tag{A9}$$

where differentiation is indicated with standard notation, ε is the neutrino energy, $s \in \{v_e, \bar{v}_e, v_x\}$, $E_{s\varepsilon}$ is the radiation energy density spectrum (zeroth moment), $F_{s\varepsilon j}$ is radiation flux spectrum (first moment), $P_{s\varepsilon i}^j$ is the radiation pressure tensor (second moment), $Q_{s\varepsilon ji}^k$ is the heat tensor (third moment), $\alpha = \exp(\phi/c^2)$, and the other variables have their standard meanings. ϕ is the gravitational potential.

 G^e and G_j^m are the main terms to add in order to include gravitational redshifts (Rampp & Janka 2002; Shibata et al. 2011). They are given by

$$G^{e} = -\mathbf{F}_{s\varepsilon} \cdot \nabla \phi / c^{2} + \nabla \phi / c^{2} \cdot \partial (\varepsilon \mathbf{F}_{s\varepsilon}) / \partial \varepsilon,$$

$$\mathbf{G}_{j}^{m} = -E_{s\varepsilon} \nabla_{j} \phi + \nabla_{i} \phi \cdot \partial (\varepsilon \mathbf{P}_{s\varepsilon j}^{i}) / \partial \varepsilon,$$

where $\nabla_j \phi/c^2 = -g_j/c^2$, and one must do the contravariant/covariant raising or lowering according to the metric. Notice that the last terms in the equations for G^e and G^m_j integrate out to zero when one integrates over energy groups, leaving the terms analogous to the ' $\rho v \cdot g$ ' and ' ρg ' work and force terms.

The gravitational potential, ϕ , is generally taken to be the 'GR-corrected' monopole term (ϕ_{TOV}). There are a variety of ways to approximate this, and the source for this approximation is Marek et al. (2006). Many people use their 'Case A', as do we, though they say their 'Case B' is also very good. The relevant equations are

$$\frac{\mathrm{d}\phi_{\text{TOV}}}{dr} = G^{\frac{m_{\text{TOV}} + 4\pi r^3 (P + P_{\nu})/c^2}{r^2 \Gamma^2}} \left[\frac{\rho + E/c^2 + P/c^2}{\rho} \right],\tag{A10}$$

$$\Gamma(r) = \sqrt{1 + v^2/c^2 - \frac{2Gm_{\text{TO}}(r)}{rc^2}},$$
(A11)

$$\frac{\mathrm{d}m_{\mathrm{TOV}}}{\mathrm{d}r} = 4\pi r^2 \left(\rho + E/c^2 + \frac{v \cdot F_{\nu}/c^2}{\Gamma} \right) \Gamma \quad \text{(Case A)},\tag{A12}$$

$$\frac{\mathrm{d}m_{\mathrm{TOV}}}{\mathrm{d}r} = 4\pi r^2 \rho \quad (\mathbf{Case} \, \mathbf{B}),\tag{A13}$$

where ρ is the rest mass density, P_{ν} is the total neutrino pressure, E is the total matter internal energy density, P is the matter pressure, V is some averaged radial speed, E_{ν} is the total neutrino energy density, and E_{ν} is the total neutrino flux. If one is using a multipole expansion to derive the potential, then the potential used is

$$\phi_{\text{eff}} = \phi - \bar{\phi} + \phi_{\text{TOV}}, \tag{A14}$$

where ϕ is the multipole Newtonian potential, $\bar{\phi}$ is the monopole Newtonian potential, and ϕ_{TOV} is the monopole TOV potential. Note that this equation merely subtracts out the monopole term from the total Newtonian potential, and then adds it back, corrected for the GR effects in the approximate way suggested by Marek et al. (2006).

So, one needs to calculate the total pressure, energy density, and flux of the neutrinos, calculate $\langle v^2/c^2 \rangle$ as a function of radius, and then integrate radially/spherically to get m_{TOV} and ϕ_{TOV} . All the non-monopolar potential contributions (if included) are Newtonian; only the monopole term is adjusted approximately for GR. This correction to the monopolar potential used in the matter momentum equation is likely the dominant effect of GR. However, the 'GR-corrected' transport scheme above incorporates the neutrino energy redshifts, as well as the time dilation. In the steady-state, zero-motion limit, the total luminosity $\times \exp(2\phi/c^2)$ is a constant, as it should be (note the factor of 2).

APPENDIX B: NEUTRINO-MATTER INTERACTIONS FOR THE SUPERNOVA PROBLEM

A comprehensive set of neutrino–matter interactions is implemented into FORNAX, and these are described in Burrows, Reddy & Thompson (2006). They include neutrino–nucleon scattering and absorption and neutrino–nucleus scattering with ion–ion correlations, weak screening, and form-factor corrections. For the neutrino–nucleon scattering cross-sections, we use equation 24 of Burrows et al. (2006) and for the charged-current absorption cross-sections (i.e. $v_e + n \rightarrow p + e^-$ and $\bar{v}_e + p \rightarrow n + e^+$) we follow the approach described in sections 3.1 and 3.2 of Burrows et al. (2006). Emissivities are calculated to be consistent with Kirchhoff's law of detailed balance, as described with equations 7 and 8 of Burrows et al. (2006). The latter incorporates the stimulated emission term for fermions, which in other formulations (cf. Bruenn 1985) is equivalent to Pauli blocking.

The weak magnetism and recoil corrections for both absorption and scattering are incorporated as multiplicative factors, using the linear fits in neutrino energy of Horowitz (2002). The linear fits are accurate below ~ 100 MeV for ν_e s and ~ 50 MeV for $\bar{\nu}_e$ s, but deviate at higher neutrino energies. Nevertheless, higher energy ν_e s reside only in the core. Moreover, there are effectively no higher energy $\bar{\nu}_e$ s in the supernova core. The degeneracy of ν_e s that results from lepton trapping also results in a positive ν_e chemical potential, and, hence, a negative $\bar{\nu}_e$ chemical potential. Such a negative potential exponentially suppresses $\bar{\nu}_e$ s. Where the $\bar{\nu}_e$ s can finally achieve significant occupancy, the temperatures and densities are too low to produce many $\bar{\nu}_e$ s above ~ 60 MeV. The ν_μ s do not experience such Boltzmann suppression, but are thermally produced, and, hence, given the core temperatures, are not produced in significant numbers above ~ 100 MeV. Be that as it may, we have also implemented the fully non-linear weak-magnetism and recoil formalism into FORNAX, done side-by-side comparison simulations in 1D, and found that the hydrodynamic and radiation results are almost identical. For the ' ν_μ ' neutrino–nucleon scattering, we use the average of the weak magnetism and recoil corrections for the neutrino and antineutrino types.

Inelastic neutrino–nucleon scattering is handled using a modified version of the Thompson, Burrows & Pinto (2003) approach. A comprehensive discussion of the equations and techniques we employ to handle inelasticity in both neutrino–nucleon and neutrino–electron scattering is found in Section 4 of Burrows & Thompson (2004). The integrals for the dynamic structure functions for inelastic neutrino–electron scattering are handled relativistically, as in Reddy et al. (1999) and the equations on pages 144–148 of Burrows & Thompson (2004). As in the case of inelastic scattering off nucleons, all integrals for inelastic neutrino–electron scattering are done numerically with quadratures, and the results are tabulated in large tables for use during simulation when inelasticity and redistribution are turned on (as they are in this work). This involves as an intermediate step the numerical calculation of polylogarithmic functions. Neutrino sources and sinks due to nucleon–nucleon bremsstrahlung and electron–positron annihilation are included, as described in Thompson, Burrows & Horvath (2000). We also include the many-body correction to neutrino–nucleon scattering of Horowitz et al. (2017), which is a variation of the formalism of Burrows & Sawyer (1998) extended to lower densities. This correction, which slightly decreases the scattering rate at progressively higher densities, has been shown to support the 'explodability' of supernova models and is physically well motivated. A corresponding correction for charged-current absorption on to nucleons has not been calculated in full (Roberts & Reddy 2017), nor included in FORNAX, but could be of equal relevance. For electron capture on nuclei, of importance during the infall phase, we employ the rates of Juodagalvis et al. (2010).

This paper has been typeset from a TeX/LATeX file prepared by the author.